An integrative experimental and computational twin modeling approach to understand clonal dynamics in the normal liver

Dirk Drasdo, Jieling Zhao

A digital liver twin demonstrating the interplay between biomechanics and cell kinetics can explain fibrotic scar formation

Jieling Zhao[1,2†], Seddik Hammad[3,4†], Mathieu de Langlard[2], Pia Erdoesi[3], Yueni Li[3], Paul Van Liedekerke[2], Andreas Buttenschoen[5], Manuel Winkler[6,7], Sina W. Kürschner[6,7], Philipp-Sebastian Koch[6,7], Niels Grabe[8], Jan G. Hengstler[1], Matthias P. Ebert[9,10,11], Steven Dooley[3*], Dirk Drasdo[1,2*]

[1]*Leibniz Research Centre for Working Environment and Human Factors, Technical University of Dortmund (IfADo), Dortmund, Germany*. [2]*National Institute for Research in Computer Science and Automation (INRIA de Saclay), Palaiseau, France.* [3]*Molecular Hepatology Section, Department of Medicine II, Medical Faculty Mannheim Heidelberg University, Mannheim, Germany*. [4]*Department of Forensic Medicine and Veterinary Toxicology, Faculty of Veterinary Medicine, South Valley University, 83523-Qena, Egypt.* [5]*Mathematics Department, University of British Columbia, Vancouver, Canada.* [6]*Department of Dermatology, Venereology and Allergology, University Medical Center and Medical Faculty Mannheim, Heidelberg University, Mannheim, Germany.* [7]*European Center for Angioscience, Medical Faculty Mannheim, Heidelberg University, Mannheim, Germany.* [8]*Hamamatsu Tissue Imaging and Analysis Center (TIGA), BIOQUANT, University Heidelberg, Heidelberg, Germany.* [9]*Department of Medicine II, Medical Faculty Mannheim Heidelberg University, Mannheim, Germany.* [10]*Mannheim Institute for Innate Immunoscience (MI3), University Medical Center Mannheim, Medical Faculty Mannheim, Heidelberg University, 68167-Mannheim, Germany.* [11]*Clinical Cooperation Unit Healthy Metabolism, Center of Preventive Medicine and Digital Health, University Medical Center Mannheim, Medical Faculty Mannheim, Heidelberg University, 68167-Mannheim, Germany.* †These two authors contribute equally to this work ***Corresponding authors:** steven.dooley@medma.uni-heidelberg.de dirk.drasdo@inria.fr

Abstract

The formation of liver fibrosis patterns is a complex dynamic and multi-cellular process that can only be marginally investigated experimentally. A digital liver twin model is warranted, as it permits integration of multiple mechanisms and study of consequences upon their modulation. We developed a computational liver model on chronic injury-mediated formation of septal fibrosis that is based on experimental iteration. This liver "digital twin" (DT) constitutes a "model" of the reality, closely reproducing the spatial-temporal pattern of hepatocytes, hepatic stellate cells (HSC), macrophages (Mph) and collagen fibers through literature and quantitative imaging of mouse experiments. The DT represents liver tissue microarchitecture containing ECM networks, hepatocytes, blood vessels, non-parenchymal cells, and cell-cell communication. The DT can precisely simulate formation of septal fibrosis and predicts that attraction of activated hepatic stellate cells (HSC) and macrophages (Mph) is controlled by spatial-temporal damage associated molecular patterns (DAMPs) released from CYP2E1 expressing hepatocytes due to CCl_4-induced injury. In addition, undamaged hepatocytes proliferate to replace the dead ones, thereby mechanically compressing the fibrotic collagen network into “wall”-like shapes. The DT is validated by perturbations, like lacking hepatocyte proliferation, HSC migration or Mph phagocytosis. Importantly, simulations assuming loss of CYP2E1 match experimental data from mice with deleted transcription factor GATA4 in endothelial cells that present with decreased CYP2E1 expression and disturbed distribution pattern in hepatocytes. Simulations and biology both show diffuse perisinusoidal instead of bridging fibrosis. In conclusion, we have generated a DT that can simulate septal fibrosis formation upon liver damage.

Introduction

Chronic liver diseases (CLD) have variant etiologies, including viral and other infections, autoimmune activities, alcohol consumption, mal/overnutrition, cholestasis, drug (ab)use or genetic abnormalities. Irrespective of the underlying etiology, chronicity reflects a long history of parenchymal cell injury and a tissue response switching between regeneration, inflammation, and fibrosis (**Pinzani and Rombouts, 2004**). Fate decisions of hepatocytes upon perturbation depends on their localisation inside "zones" of the liver lobule, the smallest repetitive anatomical unit. For example, repetitive treatment of mice with CCl_4 leads to pericentral hepatocyte damage, since only these cells express the Cytochrome P450-enzymes Cyp2E1 and Cyp1A2, which metabolize CCl_4 to cell damaging products. The consequence of repetitive CCl_4 damage is formation of pericentral/septal fibrosis. If, however, the liver suffers from cholestasis, damage is initially caused by toxic levels of bile acids, beginning with the cholangiocytes, progressing via the periportal hepatocytes, and leading to periportal/biliary fibrosis. All CLD have in common that the wound that arises from damage is “repaired” by excessive extracellular matrix deposition, which in case of multiple rounds of damage finally leads to tissue scarring towards cirrhosis (**Kisseleva and Brenner, 2021**), the major risk factor for hepatocellular carcinoma (Moon et al. 2019). During the past decades, research on liver fibrogenesis mainly focused on molecular and cellular mechanisms (**Seki and Brenner, 2015**; **Kisseleva and Brenner, 2021**), suggesting a widely accepted concept, where injured hepatocytes send out signals, so called damage associated molecular patterns (DAMPs) towards the surrounding liver cells. Liver macrophages (Mph) produce fibrogenic cytokines such as TGFβ and PDGFβ to activate and recruit hepatic stellate cells (HSC), which produce and deposit extracellular matrix (ECM) proteins (**Seki and Schwabe, 2015**; **Higashi et al. 2017**). Mphs comprise the liver resident Kupffer cells and recruited monocyte derived Mphs, and have diverse functions in onset, progression and regression of liver fibrosis, by switching between inflammatory and restorative phenotypes (**Ramachandran et al. 2012**; **Krenkel and Tacke 2017**; **Krenkel et al. 2019**; **Papachristoforou and Ramachandran 2022**). HSCs also display significant plasticity and are able to switch between quiescent (qHSC), differentially activated (aHSC) and reverted subtypes (rHSC) (**Kisseleva et al. 2012**; **Krenkel et al. 2019**; **Filliol et al. 2022**). During fibrosis regression in phases without damage, aHSCs are depleted, approximately 50% by cell death and 50% by reversion to quiescence phenotype (**Kisseleva et al. 2012**). Changes in the cellular phenotype of HSCs are induced by molecular signals and by alterations of the ECM with mechanical consequences on tissue stiffness and viscoelasticity (**Huang et al. 2012**; **Török et al. 2022**; **Caliari et al. 2016**). Despite these and other investigations (**Hernandez-Gea and Friedman, 2011**; **Pinzani and Luong, 2018**; **Parola and Pinzani, 2019**; **Kisseleva and Brenner, 2021**), pattern formation in fibrosis is not well understood. A better understanding of the formation of specific fibrosis patterns, however, would be helpful to design the treatment strategy to prevent liver fibrosis progression to cirrhotic nodule. Eventually, the presentation of fibrosis progression or reversion is tightly orchestrated by spatial-temporal distribution of ECM producing (HSC) and degrading (Mph) cells, and the respective cell numbers and their location will finally also be decisive for the variant fibrosis pattern formation discussed above.

In patients, knowledge on the dynamics of liver disease development, progression and regression can only be collected indirectly via longitudinal blood sampling or by non-invasive imaging methods, like MRI or ultrasound. Blood parameters do not exclusively relate to disease activities in the liver, and imaging can up to date only provide morphological and biomechanical tissue properties at super-lobular scales. Information about the liver micro-architecture is collected from resected or biopsied livers that are available from only very few selected time points. Time course data on the dynamics of cellular fate changes are therefore principally generated from animal disease models, but these still do not permit simultaneous measurement of all possibly involved process variables, therefore often fail in establishing unique cause-effect relationships, due to the complexity of the system. To address this, we developed a computational digital twin (DT) to simulate hypothesized mechanisms and to assist in data interpretation and data acquisition design, where the complexity of the system interplay does not permit unambiguous conclusions. With the DT, we are able to overcome the bottleneck that the system of interest is not sufficiently amenable to manipulations and measurements, as is the case in human chronic liver disease.

The presented DT is able to resolve the spatial-temporal organization of tissue microarchitecture as determined from histological tissue samples or by intravital imaging, both requiring invasive interventions. It does this by representing each cell individually within a cell (agent)-based simulation approach, either at high resolution resolving cell shape in space regions, where interactions with the extracellular matrix must be considered, or at low resolution sufficiently far away from the liver tissue damage zone. High resolution cell models permit a higher accuracy of biomechanics at the expense of longer simulation times (e.g. **Odenthal et al. 2013**; **Kim et al. 2018**; **Winkler et al. 2019**; **Van Liedekerke et al. 2019, 2020**), while low resolution models are less accurate, but computationally more efficient (e.g. **Van Liedekerke et al. 2015**). The DT is based upon consistent use of computing forces of cell and ECM displacement and deformations, whereby ECM is mimicked as linked strings of polymer-like objects similar as in (**Ban et al. 2018**; **Ronceray et al. 2016**; **Stein et. al. 2008**). Computational models have already been successfully used to predict cellular and tissue responses on several aspects of acute and chronic liver injury in mice and patients and were able to integrate complex interactions and system components with increasing realism (**Hoehme et al., 2010**; **Lara et al. 2014**; **Dutta-Moscato et al. 2014**; **Friedman and Hao, 2017**; **Adhyapok et al. 2020**; **Hoehme et al. 2023**; **Dichamp et al. 2023**; **Zhao et al. 2023**). Some of them resolve tissue microarchitecture, representing cells individually (**Hoehme et. al. 2010**; **Dutta-Moscato et al. 2014**; **Adhyapok et al., 2020**; **Hoehme et al. 2023**; **Dichamp et al. 2023**; **Zhao et al. 2023**), others study cell densities and molecular concentrations averaged over spatial scales at which the individual organization of cells can be neglected within continuum models (**Friedman and Hao, 2017**), or even using statistical models discarding any space structure (**Lara et al. 2013**). At the tissue microarchitectural level, some models consider a rigid scaffold structure leading to cellular automaton models, which does not permit gradual cell displacements or deformations, but are computationally highly efficient (**Dutta-Moscato et al. 2014**; **Adhyapok et al. 2020**), while others resolve biomechanical cell and tissue properties at the expense of long simulation times but generate simulated tissue structures highly reminiscent of 3D histological image reconstructions (**Hoehme et al. 2010**; **Hoehme et al. 2023**; **Dichamp et al. 2023**; **Zhao et al. 2023**).

The current DT belongs to the last class of models and simulates liver fibrogenesis, a highly dynamic, tightly controlled process that comprises continuous communication between hepatic cell types and structural liver components. Many molecular aspects have been experimentally delineated, whereas some key aspects, such as the biomechanical control of the interplay between hepatocytes, HSC, Mph and the collagen fibres have not been explicitly considered previously and are subject of the presented work.

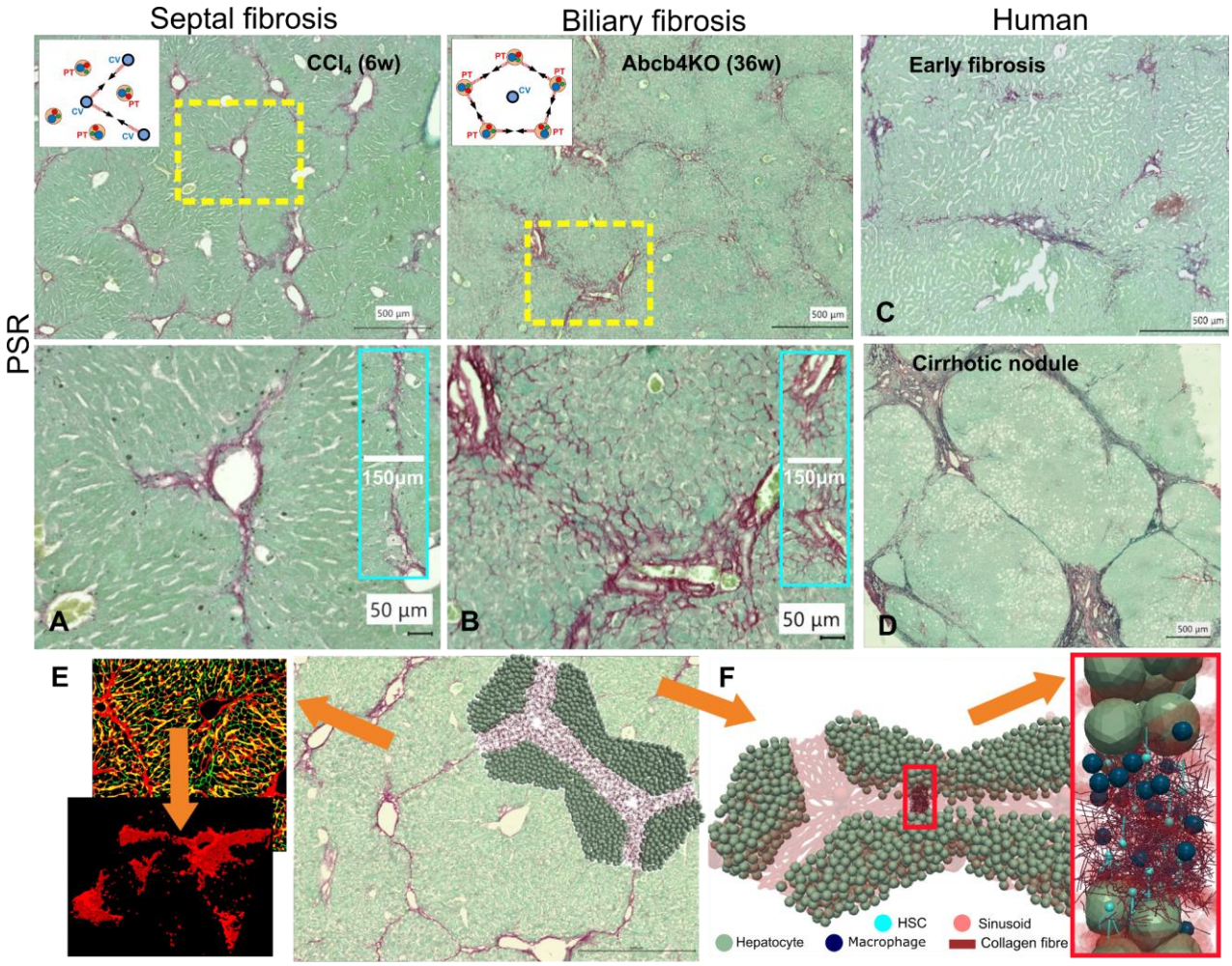

Figure 1. **Liver fibrosis patterns - Pathomorphology in murine and human specimens and in a liver Digital Twin.** (A) Pericentral or septal fibrosis of 6 weeks CCl_4 exposed livers. (B) Biliary/portal fibrosis of 36 weeks old Abcb4*KO* mice. (C) Early stage human liver fibrosis. (D) Representative cirrhotic nodule. (E) The view of the fibrotic wall (red) constructed from confocal images of fibrotic liver. (F) Experimental data derived computational model including hepatocytes, hepatic stellate cells (HSC), macrophages, sinusoids, and collagen fibres. Scale bars are 500µm and 50µm for overviews and closeups, respectively. CV, central vein; PV, portal vein; CCl_4, carbon tetrachloride; PSR: picro-sirius red.

Materials and Methods

Animal experiments

Adult C57Bl/6N male mice (Janvier labs; France) were housed three per cage in a temperature-controlled (24°C) room with a 12-h light/dark cycle. Mice were given *ad libitum* access to water and laboratory diet (Ssniff, Germany). Mice were exposed to carbon tetrachloride (CCl_4; Sigma-Aldrich, Cat. no. 319961) in a dose of 1.6 g/kg body weight (**Zellmer et al. 2010**; **Hammad et al. 2014**), either at a single (acute) or repeated dose. To track regeneration and wound healing parameters upon acute intoxication, mice were exposed to a single dose of CCl_4. Blood and liver samples were harvested at 0, 1, 2, 3, 4, 6, 16, and 30 days post CCl4 injection. Liver fibrosis was induced by two doses of CCl_4 /week for 3 weeks (**Hammad et al. 2017**). Three days after the last CCl4 injection, blood and livers were harvested. All experimental protocols with animals were carried out in full compliance with the guidelines for animal care and were approved by the Animal Care Committee from the German government (Animal permission number: 35.9185.81/G87/10 and 35.9185.81/G-216/16).

Histological staining and quantification. Stainings were performed on paraffin slides (3µm) for hematoxylin and eosin (H&E) and Sirius red staining and with fast green staining (according to Lopez-De Leon and Rojkind, 1985). Further, immunohistochemistry (IHC) using anti-CYP2E1 (Sigma-Aldrich, HPA009128, raised in rabbit, 1:50), anti-mouse F4/80 (BioRad, MCA497, raised in rat, dilution 1:2000), anti-Ki-67 (Cell Signaling Technology,

CST#12202, raised in rabbit, dilution 1:200), anti-CK19 (ProteinTech, 14965-1-AP, raised in rabbit,1:100), anti-BrdU (BioRad, MCA2060, raised in rat, dilution 1:250) and anti-α-smooth muscle actin (α-SMA; Abcam, Ab5694; raised in rabbit, dilution 1:100) was performed. Image acquisition was performed using an Aperio 8 slide scanner (Leica). A minimum of 10 high-power fields were captured for image analysis. The positive areas were quantified as a brown area percentage or nuclei number by Image J or manually, respectively (5-7 fields at least per slide, 10X).

Mathematical model: the digital twin

The digital twin considers each individual hepatocyte, hepatic stellate cell, and macrophage as individual model units, models sinusoids in space and time, and extracellular matrix bundles. Each hepatocyte and macrophage is represented by one component, while hepatic stellate cells, sinusoids, and ECM bundles are mimicked as composed of many model components. The movement and interaction of each model component is modeled by a force balance equation. The force balance equations are updated simultaneously for all model components (e.g. hepatocytes, HSC, Mph and the collagen fibres) by solving a system of coupled equations, one for each component, to represent all forces exerted on each component: $\sum \square_{\square\square\square} + \square_{\square\square\square} + \square_{\square\square\square} = 0$. Here $\square_{\square\square\square}$, $\square_{\square\square\square}$, $\square_{\square\square\square}$ are the friction force with the environment, deformation force, and adhesive force, respectively (see details in Supplementary Information). In total, half a million equations had to be solved to simulate weeks of real time. Due to the long simulation times with one time step of the order of 10^{-3} s, we had to limit it to one single part of the damage region along the CV-CV axis of two neighboring lobules sections (red box in **Fig. 1F**). In addition to direct interactions by physical forces, cells can communicate via diffusive signals. For these, reaction-diffusion equations were solved.

*Detailed Materials and methods are described in the **Supplementary Information**.*

Results

(I) Different etiologies of liver damage induce variant patterns of fibrosis

In a first step we compared fibrosis patterns of different etiologies to generate possible hypotheses on the generation of pericentral/septal fibrosis. Liver fibrosis patterns are present as septal, biliary, or pericellular types. In case of septal fibrosis, liver damage occurs in the pericentral compartment and then bridges between central veins (CV) of contiguous lobules. Repetitive (chronic) CCl_4 intoxication is a well-studied animal model for septal fibrosis.

Picro-sirius red (PSR) staining of the liver after 12 CCl_4 injections during 6 weeks shows bridging fibrosis between CVs, forming so-called "pseudolobules" (**Fig. 1A**). In biliary fibrosis, exemplified by the Abcb4*KO* mouse, collagen deposition starts periportal and bridges towards the adjacent portal veins in progressed disease (PV; **Fig. 1B**). In CCl_4-induced fibrosis, crosslinked collagen fibers form a thin and sharp wall-like structure, whereas in the livers of Abcb4*KO* mice, collagen fibers remain scattered and built a periportal fibrosis area that bridges as a broader streetnet between portal fields (**Fig. 1B**). Early liver fibrosis in humans appears perivenous (septal or biliary) (**Fig. 1C**) according to etiological factors, forming cirrhotic nodules in late disease stages (**Fig. 1D**). The view of the accumulated collagens of septal fibrosis in 3D shows that they form into a wall-shape structure (**Fig. 1E**). In conclusion, fibrosis patterns vary depending on disease etiology and type of injury. Currently, knowledge on the underlying mechanisms that explain the respective kind of ECM deposition pattern is limited. The sharp compression of ECM towards a narrow streak that is connecting two lobules, as present in CCl_4 fibrosis, cannot be found in any disease stage of the Abcb4*KO*-mouse, but is representative for advanced fibrosis in human patients e.g. from NASH (**Fig. 1D**). We analyzed the spatial distribution of CCl_4 metabolising (CYP2E1+) hepatocytes in correlation to collagen deposition during the dynamics of liver fibrosis by (immuno)staining of serial sections with PSR, CYP2E1 and CK19, the latter indicating bile duct epithelial cells representative for periportal locations. Thus, we observed that the fibrotic wall in CCl_4-induced fibrosis is generated between the of CYP2E1+ hepatocytes, which localize around and form layers between CVs, upon repetitive CCl_4 injections (**Supplementary Fig. 1**). This indicates that the observed septal fibrosis pattern formation is associated with the dynamics of metabolic activity (CYP2E1 expression), damage, and proliferation of hepatocytes in response to the toxin-induced injury. This guides us to the ***main hypothesis***, that the sharp fibrotic wall in septal fibrosis is formed by compression of an initially scattered ECM, driven by mechanical forces that are exerted by the proliferating hepatocytes.

In order to handle the complexity of this scenario, and to be able to continuously integrate and exchange possible drivers of septal fibrosis patterns formation, we selected a systems biology approach and developed a minimal liver Digital Twin (DT) that is able to simulate observed and hypothesized process steps leading to fibrotic scar formation, including intracellular signal processing, cell-cell communication and tissue biomechanics. The key components of the DT include different liver cell types, sinusoids, and collagen fibres (**Fig. 1F**), integrated in a two-hepatic lobule model for the process of fibrogenesis. We selected a two-liver lobules DT, since the minimal fibrotic wall unit in septal fibrosis bridges two central veins **(Fig. 1F**). The micro-architecture and cell composition in the DT space unit was developed as an experimental equivalent of the starting state prior to the first administration of CCl_4.

Next, we collected data to construct the spatial-temporal microarchitectural DT of liver fibrosis. The pursued strategy was to calibrate the DT with data on acute liver injury after a single dose of CCl_4 and predict with the so calibrated DT the remodeling of liver tissue microarchitecture after repeated doses of CCl_4. The predictions were then confronted with the experimental findings after repeated CCl_4 injections (twice a week at days 3 and 7 of each week for 6 weeks).

(II) Experimental data-driven generation of a computational microarchitectural model for the formation of fibrotic scars resulting from acute drug-induced liver injury (DILI) following a single CCl_4 injection.

The components of the DT are stepwise introduced, commencing with the tissue microarchitecture, then extending to the hepatocytes presenting in various states, e.g. physiological, damaged (or dead), and proliferating. Following this, non-parenchymal cells, such as hepatic stellate cells and

macrophages, are incorporated, along with the extracellular matrix. Each model element is outlined with its spatial depiction and potential dynamics. The chosen model constituents were crafted based on quantitative imaging of their designated structures.

A) Sinusoidal scaffold:

Previous research indicates that the sinusoidal network within the liver, often referred to as liver capillaries, sustains damage following CCl_4 treatment, yet retains its principal structural framework (Hoehme et al., 2010). Consequently, we utilized this framework as a foundational structure for the two-lobule DT. The sinusoids were conceptualized as semi-flexible chains of small spheres interconnected by springs (depicted in transparent red, **Fig. 1F**). This model representation enables the formulation of force balance equations for each sphere within the sinusoidal network, similar in structure to those governing the cells. Such a framework facilitates the simulation of sinusoid displacements. When neighboring cells exert compressive forces on a sinusoid, this reduces the apparent thickness of the sinusoidal diameter, thus emulating a compressive effect.

B) Hepatocytes:

To experimentally determine the fate and localization of different liver cell types, we utilized mouse livers from healthy controls and those harvested 3 days after a single CCl_4 injection. This served as a reference state to establish the initial configuration of the dynamic system. Day 3 was chosen, as it marked the initiation of fibrosis development, starting with administration of the second dose of CCl_4. Following a solitary CCl_4 injection, the liver undergoes complete regeneration of the lesion by day 7 (**Hoehme et al. 2010**).

We quantified the proportions of healthy, necrotic, CYP2E1-expressing, and proliferating (BrdU-labeled) hepatocytes in the reference state. Initially, pericentral hepatocytes experience necrosis due to CCl_4 metabolism (8.86±2.45% of the total area shows CYP2E1 positivity). Conversely, midzonal and periportal hepatocytes maintain a healthy appearance throughout the process. This was demonstrated and quantified on day 3 through HE and IgG staining (**Fig. 2A, B; Supplementary Fig. 2A, B**). Notably, the highest fraction of necrotic cells is observed 1 day after the initial dose, consistent with prior findings (**Hoehme et al. 2010**).

Vanishing pericentral hepatocytes were confirmed by the complete loss of CYP2E1 positivity, a decrease in Cyp2e1-mRNA expression by day 2, and elevated plasma alanine transaminase (ALT) and aspartate transaminase (AST) levels on days 1, 2, and 3. Enzyme levels normalize as regeneration progresses (**Fig. 2D**). Necrotic regions nearly close by around day 5. CYP2E1 mRNA and protein expression do not fully return to their original levels and patterns, at least until day 30 in the regenerated liver. Moreover, a layer of midzonal peri-necrotic hepatocytes starts expressing CYP2E1 on day 3, forming a wedge-shaped line connecting adjacent central veins (**Fig. 2A**). The number of central veins connected by CYP2E1-positive cells remains elevated until day 30 in the regenerated livers (**Fig. 2C**). The remaining hepatocyte fraction on day 3 exhibits an increased count of BrdU/Ki-67 positive cells/nuclei, which are not uniformly distributed within the hepatic lobule, but are more prevalent in peri-necrotic areas (**Fig. 2A, B, E, F; Supplementary Fig. 1A**).

In the DT, each hepatocyte was individually modeled as a single unit, whereby the spatial resolution of the cell shape was made dependent on its proximity to the emerging necrotic lesion. Hepatocytes close to the lesion, interacting with the ECM fiber network during fibrosis formation, were simulated using a "deformable cell model (DCM)" that explicitly tracked cell shape changes (**Van Liedekerke et al. 2020**; **Fig. 2G, Supplementary Movie 1**). Hepatocytes further away, not in contact with newly synthesized collagen fibers, were modeled using a "center-based model (CBM)", where forces on the cell were represented as forces on the cell's center. For simplicity, the shape of a cell in CBM was depicted as a sphere, as this is the shape the cell would assume in isolation.

CYP2E1-positive hepatocytes (yellow) are connecting two CV (**Fig. 2A**). CYP2E1-negative hepatocytes outside the lesion were classified as damage-resistant cells (green, **Fig. 2G**). CYP2E1-positive hepatocytes underwent cell death (necrotic cells, brown) following CCl_4 injection. A portion of the remaining hepatocytes that proliferate (blue) to close the necrotic lesion was stochastically selected based on the time point after CCl_4 treatment and their distance from the lesion. The spatiotemporal proliferation pattern was inferred from quantifying Ki-67-positive cells, as previously performed (**Hoehme et al. 2010**). BrdU staining predominantly served to illustrate a higher number of proliferating hepatocytes surrounding the necrotic lesions.

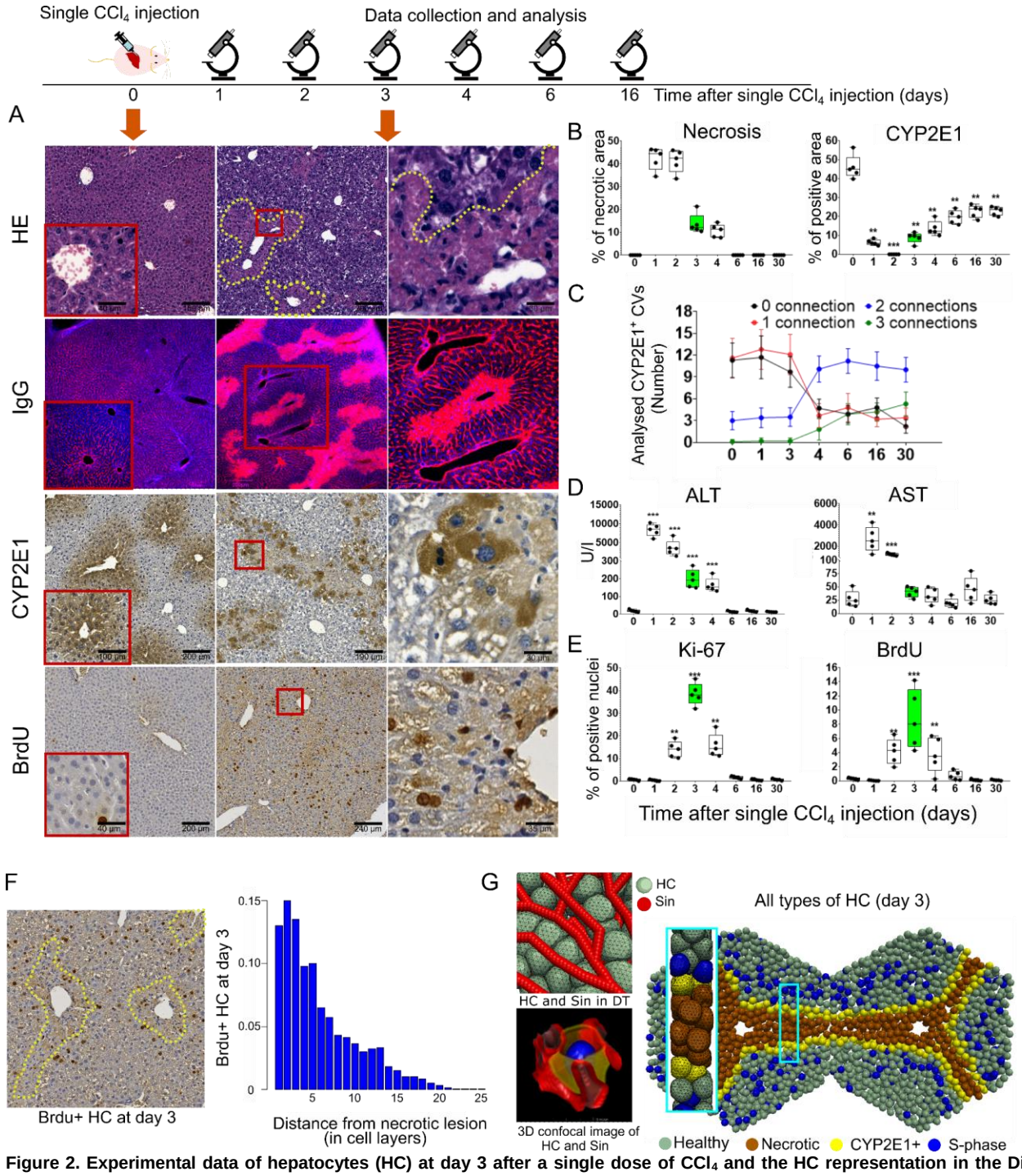

Figure 2. Experimental data of hepatocytes (HC) at day 3 after a single dose of CCl_4 and the HC representation in the Digital Twin (DT). (A) Histopathological investigations at day 3 after a single injection of CCl_4; HE (light purple, lesion boundary shown as dashed yellow line), IgG for necrosis/cell death, CYP2E1, the CCl_4 metabolizing enzyme, and BrdU, for nuclei in S-phase. (B-E) Quantification of necrotic area, CYP2E1, number of CV-CV connections by CYP2E1+ hepatocytes, blood levels of liver enzymes ALT & AST, Ki-67, and BrdU after single CCl_4 injection, respectively. (F) Example of BrdU stained hepatocyte nuclei (dark brown, lesion boundary shown as dashed yellow line) (left). (Right) The fraction of BrdU-positive hepatocytes versus the distance of the lesion boundary (the yellow line) at day 3 after a single CCl_4 injection. (G) Components of the DT, including hepatocytes and sinusoidal system (Sin). The left side displays a few hepatocytes in the deformable cell model embedded in a sinusoidal network

structure (upper picture), and a reconstructed hepatocyte from confocal microscopy (lower picture). Data were collected from 5 mice per time point. * P <0.05, ** P <0.01, *** P <0.001.

C) Non-parenchymal cells and the extracellular matrix (ECM):

Next, a spatial-temporal visualization with a detailed analysis of the kinetics was conducted on HSC, recognized for their involvement in both regeneration and fibrogenesis, following a single CCl_4 injection. The assessment encompassed a spatiotemporal approach, utilizing α-SMA, desmin, and PSR as markers to evaluate aHSC and total (aHSc plus qHSC), alongside ECM deposition (**Fig. 3A-C; Supplementary Fig. 3**). The spatial distribution of α-SMA-positive cells in regions between CVs at day 3 corresponds to a width of about four hepatocyte layers (80 µm, the size of the lesion; **Supplementary Fig. 4**). Notably, he stained area fraction for both desmin (5.54±0.48%) and α-SMA (3.73±1.57%) peaked at day 3. Additionally, RNA expression levels of desmin and α-Sma were found to be upregulated on day 3.
The presence of PSR-positive fibers was mainly observed in the tunica adventitia of larger blood vessels, namely the CV, PV, and hepatic artery. Conversely, small, isolated, and scattered ECM fibers were evident on day 3 within necrotic areas. This observation aligns with the increased mRNA levels of Col1α1 and Col1α2 around this specific time point **(Fig. 3D**). Notably, an excessive deposition of ECM has not been previously reported in the context of acute toxic liver injury, and our study findings are consistent with this trend. This suggests that the isolated ECM fibers visualized within the necrotic region on day 3 are rapidly degraded following their production, ultimately diminishing over time during the process of liver regeneration.

Within the DT, each HSC is conceptualized as a nucleus sphere linked to several chains of elastic springs, which represent the elongated projections of the cells. qHSCs are denoted in cyan, while aHSCs are depicted in light brown (dashed red boxes **Fig. 3F**). In the model, solely the aHSCs are endowed with the capacity to generate collagen fibers. These fibers congregate within the extracellular space, coalescing to form an intricate network (elaborated further in the Methods section with reference *collagen fiber model*).
The ECM network is portrayed as an array of semi-flexible spring chains. Each chain comprises interconnected beads that necessitate energy to bend and compress along the bundle, effectively simulating their mechanical attributes (indicated in purple, as shown in **Fig. 3F**; **Supplementary Fig. 5A**). The density of the ECM network is contingent on the density of the collagen fibers. When the separation between two fibers falls below a specific threshold, they undergo crosslinking, illustrated by the introduction of an additional node (**Supplementary Fig. 5B**). The ECM model was fine-tuned through bending and compression experiments conducted *in vitro*, in line with the work of Yang et al. (2008) and Ferruzzi et al. (2019). This calibration process ensures congruence between the modeled ECM network and the documented mechanical responses to bending and compressive stresses (**Supplementary Fig. 5C-G**).

In the next stage, we postulated that the cumulative ECM deposition is influenced by degradation processes, such as matrix metalloproteinases (MMPs) secreted by resident macrophages (Kupffer cells), which act as ECM modulators. Consequently, we conducted an analysis of the spatiotemporal distribution of macrophage infiltration using F4/80 immunostaining. In healthy livers, F4/80-positive cells exhibited a predominantly uniform distribution within periportal (arrow 1 in **Fig. 3A**, day 0 of F4/80) and midzonal (arrow 2 in **Fig. 3A**, day 0 of F4/80) compartments, while in perivenous areas (arrow 3 in **Fig. 3A**, day 0 of F4/80), there are much fewer F4/80-positive cells (**Fig. 3A**; **Supplementary Fig. 3**). However, at days 2 and 3 following CCl_4 injection, F4/80-positive cells significantly accumulated in the necrotic regions. This injury mediated spatial distribution of F4/80-positive cells required more than 16 days to return to a normalized state. Gene expression analysis revealed upregulated Cd68, a macrophage marker, as well as ECM modulators (Tgfβ1, Mmp9, and Timp1), within the first 4 days after CCl_4 injection. Mphs engulf the bodies of necrotic hepatocytes (**Wen 2023**) and play a role in degrading collagen fibers (**Madsen et al., 2013**).
In the dynamic model, macrophages are depicted as elastic spheres (dark blue, Mph, **Fig. 3F**), which upon contact, phagocytose necrotic hepatocytes and are able to degrade collagen fibers.
In summary, the experimental findings suggest a complex interplay involving hepatocytes (healthy, damaged source of DAMPs, and proliferating), qHSC, aHSC, ECM, and macrophages, forming a minimal set of parameters to construct a dynamic model for studying the cycles of damage, regeneration/repair, and fibrogenesis after repetitive CCl_4 injections (**Fig. 3G**). Notably, a subset of aHSC is known to revert to a quiescent state by cell communication with macrophages, and present with a “reverted” phenotype that displays a so-called memory response upon challenge with a new insult, in this case from the 2nd injection of CCl_4.

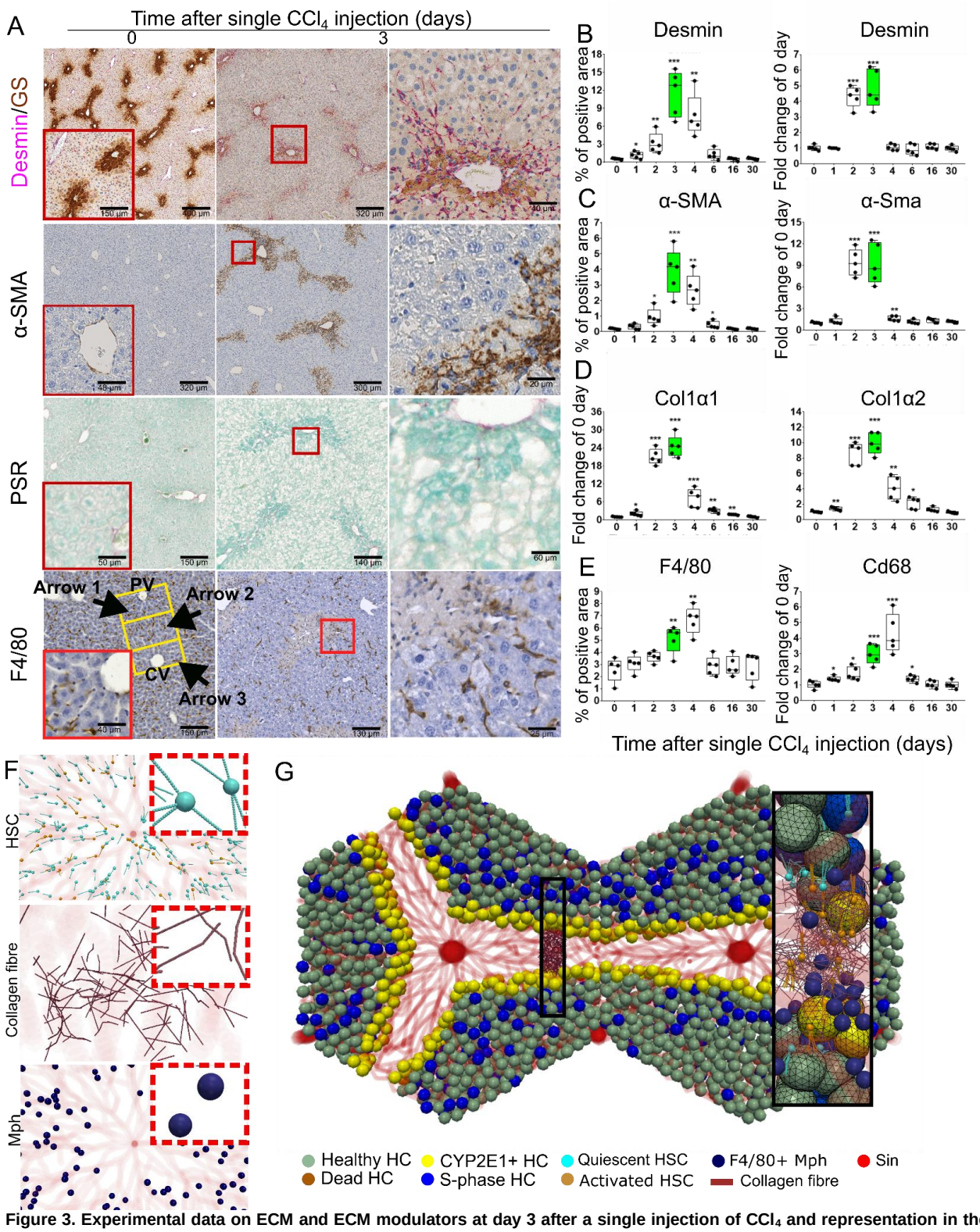

Figure 3. Experimental data on ECM and ECM modulators at day 3 after a single injection of CCl_4 and representation in the Digital Twin (DT). (A) Time-resolved histopathological data after a single CCl_4 injection, showing PSR (ECM deposition), desmin (quiescent and activated HSC), α-SMA (activated HSC), and F4/80 (stained in brown, resident Mph). Arrows 1, 2 and 3 point to F4/80-positive cells in periportal, midzonal, and perivenous regions, respectively. (B-E) Quantification of positive staining (left picture) and mRNA levels (right picture) for desmin (B), α-SMA (C), mRNA levels of

Col1α1 and Col1α2 (D), and F4/80 (positive staining)/Cd68 (mRNA level) (E). (F) Components of the DT include HSC, Mph and collagen fibers (ECM) (shown are small spatial tissue regions in the model and the model component in the inset). (G) A DT of two liver lobules that comprises all listed components. Data are shown from 5 mice per time point. * P <0.05, ** P <0.01, *** P <0.001.

(III) Implementation of Processes Pertaining to Septal Fibrosis Formation Dynamics

Subsequent to setting up the experimental design and observations leading to fibrotic wall formation, the DT is subjected to a simulation of six CCl_4 injections over a three-week timeline (twice a week), mirroring the experimental schedule. CCl_4 injections are performed at days 0 and 3 of each week, enumerating weekdays from 0 to 6. In this scheme, injections (enumerated in parenthesis) occur at days 0 (1), 3 (2), 7 (3), 10 (4), 14 (5), 17 (6), with a last histological analysis at day 20. Each CCl_4 injection induces damage to the fraction of CYP2E1+ hepatocytes, which is always reflected by upregulated AST and ALT levels in the blood of the mice (**Fig. 4; Supplementary Fig. 6**).

In the experiments, only the cell layer adjacent to the necrotic lesion expresses CYP2E1 at day 3 after one CCl_4 injection. The necrotic areas subsequently are restored by hepatocyte proliferation, whereby importantly, the newly generated hepatocytes are all expressing CYP2E1, indicating peri-central metabolic zonation, and therewith, sensitivity for the next CCl_4 injection. CYP2E1 positive hepatocytes are now spatially organized to connect two neighboring CVs (note that the stripe of CYP2E1-expressing hepatocytes after 2, 4, or 6 injections of CCl_4 is of very similar size).

In the DT, hepatocytes filling the necrotic lesion are assumed to express CYP2E1. The reestablished CYP2E1-positive pattern guides the progression of damage over time and space, therewith shaping the spatial DAMP concentrations and ensuing responses, including recruitment of HSC and Mph, deposition of ECM, as well as compensatory hepatocyte proliferation, in order to repeatedly restore the lesion.

The proliferation profile is parameterized based on Ki-67 staining quantification on day 3 after the first CCl4 injection, consistent with previous studies (**Hoehme et al. 2010**). Experimental quantification and spatial localization of hepatocyte proliferation after repeated CCl_4 injections revealed that the healthy hepatocytes enter the cell cycle for proliferation. The proliferation rate is highest adjacent to the lesion and decreases gradually with increasing distance from the lesion (**Fig. 2F**).

In the DT, compromised CYP2E1-expressing hepatocytes are assumed to serve as the source of DAMPs, which among others attract HSC (**Supplementary Fig. 7A, B**), causing their activation and migration into the lesion. These HSCs eventually produce collagen fibres, initially distributed in a so-called “chicken wire” pattern, and captured by our model as shown in **Supplementary Fig. 7C and D**. In the experimental context, scattered fibers are observed a week after the second CCl_4 injection, which progressively organize into a well-defined fibrotic wall after 4-6 doses. The collagen deposition pattern goes along with the spatial pattern of the desmin and α-SMA expressing cell population. The temporal pattern of the mRNA expression of the ECM genes collagen 1α1 and 1α2 shows a similar increase as those of α-SMA, Cd68, Mmp9 and Timp1 at RNA and protein levels. (**Supplementary Fig. 8**). No further accumulation of HSC is found in response to doses beyond 4-6 CCl_4 injections.

The mechanism mediating spatial organization of secreted collagen fibres and its dynamic alterations to finally develop fibrotic walls is unknown. The enzyme CYP2E1, which due to mechanistic estimations is most probably shaping the overall spatial patterning of the ECM, as well as the occurrence of the ECM producers (aHSC), defined by desmin and α-SMA staining, remains relatively disperse (**Supplementary Fig. 8A**). To test our hypothesis, we simulated the entire process of repeated CCl_4-injections and the downstream events this triggers in the DT. We studied six alternative scenarios (S) of collagen fibres deposition: (S1), as single fibres; (S2), as single fibres anchored to the nearest sinusoids; (S3), as crosslinked single fibres; (S4), as crosslinked single fibres anchored to the nearest sinusoids; (S5), as collagen fibres, which are firstly deposited as single fibres and then gradually crosslinked; (S6), as collagen fibres that are firstly deposited as single fibres anchored to the nearest sinusoids and are then gradually crosslinked (**Supplementary Fig. 9A**). To investigate how sensitive the collagen network in each of the scenarios is in response to biomechanical forces exerted by proliferating hepatocytes, we first simulated a simplified lesion without HSC and Mph in a stripe inside the two-lobules system with the DT (**Supplementary Fig. 9B-D**) for a time frame of 21 days.

The total mass of collagen fibres was initialized homogeneously distributed in the lesion region. There was no fibre deposition or degradation during the simulation. All collagen fibres are generated immediately after the first CCl_4 injection. To pre-estimate the maximum density that the produced collagen adopts in the striped space, which we assume corresponds to the collagen density required for the formation of the experimentally observed fibrotic wall, different densities as described in the literature (0.4, 1.0, and 2.0 mg/mL, Stein et al., 2008) were tested in the simulations with the DT. Surprisingly, every time a wall-like fibrotic structure resulted at day 20 after 6 repeated CCl_4 injections. Nevertheless, some of the simulated scenarios exhibited variations in thickness, appearing either thinner or thicker than what was observed in the experimental data (see **Supplementary Fig. 9B-G** for details). Additional information regarding the extensive testing of various collagen densities can be found in the Supplementary Information section titled "**Organizational Structure of the Collagen Network**." This supplementary section provides detailed insights into the evaluation process of different collagen densities and their impact on the simulation results. Ultimately, scenario 5, which exhibited a collagen density of 1.0 mg/mL, closely resembled the experimental data and was chosen for further simulations and analysis. This scenario's plausibility stemmed from the concept that aHSCs generate and accumulate ECM fibers, which subsequently crosslink to form a comprehensive ECM network.

Following the selection of a plausible collagen density scenario (scenario 5) based on its similarity to experimental observations, the next step involved incorporating macrophages into the DT Model. This was done considering the dynamic changes in the numbers and distribution of F4/80-positive stained Mph (dark blue; **Fig. 3F and G**). The assumption here was that these Mphs digest collagen fibers upon contact. Consequently, in the DT, collagen fibers start being generated by aHSC after the second CCl_4 injection, followed by digestion of these fibers by Mph within the lesion.

In the DT, the interplay of ECM production (α-SMA positive cells), digestion (F4/80 positive cells), and biomechanical forces from hepatocyte division collectively modulate the thickness of the ECM network. This modulation is reflected in the changes of the gyration diameter, which captures the width of the collagen distribution, with the maximum distribution approximately aligned with the fibrotic streak connecting neighboring CV. This gyration diameter decreases from 46µm after the second CCl_4 dose to about 20µm after 6 doses of CCl_4, ultimately shaping the collagen network into a well-established fibrotic wall (**Fig. 4C**). This intricate interplay leads to the formation of the characteristic fibrotic patterns observed in experimental data (**Fig. 4D**; **Supplementary Movie 2**).

In a parallel setup mirroring the chronic liver injury scenario over 3 weeks with two CCl_4 injections per week, each CCl_4 injection results in cell death of CYP2E1-expressing hepatocytes localized in the lesion (**Supplementary Fig. 6A**). PSR staining reveals that single collagen fibers are deposited in the liver starting from day 3 after the first CCl_4 injection, gradually accumulating in the necrotic region after two doses, and coalescing into thick bundles after 4 doses (**Fig. 4E**). Following 6 doses of CCl_4, a clear wall-shaped fibrosis pattern is established, spanning between, and surrounding the CVs. This sequential order of collagen fiber accumulation, along with the spatiotemporal distribution of fibers and aHSC, is successfully simulated by the DT model (**Fig. 4D, E**). The area of PSR positive regions shown in **Fig. 4E** were quantified and shown in **Fig. 4B**. aHSCs migrate into the lesion following the first dose and accumulate over time in the region, where the wall-shaped collagen network is formed after 6 doses of CCl_4 (**Supplementary Fig.**

8A). This accumulation of aHSC is also reflected in the quantification of the α-SMA positive cell fractions over time (**Fig. 4F**).

As indicated by HE staining (**Supplementary Fig. 6A**), tissue infiltration of cells with small nuclei is observed in and around fibrotic areas. Some of these cells are Mph, whose spatial distribution follows a pattern similar to aHSC as shown by F4/80 positivity. The accumulation of positively stained Mph in the fibrotic region is confirmed by F4/80 staining after two doses of CCl_4. After 4 doses Mphs start to accumulate in wall-like patterns, linking CVs after 6 doses that in the 2D sections look like streaks (**Supplementary Fig. 8A**). Quantification of F4/80 positive cells indicates that the Mph numbers remain relatively stable after the second CCl_4 dose (**Fig. 4F**). This stability is supported by RNA data, which show no further upregulation of Cd68, Mmp9, or Timp1 expression (**Supplementary Fig. 8D**).
In the DT, it has been established that Mphs migrate toward the gradient of DAMP concentrations following the first CCl_4 dose and locate around the lesion in a scattered manner, even after 6 doses of CCl_4 (**Fig. 4D**). Furthermore, the number of Mphs in the lesion is defined by the F4/80 positive fraction (**Fig. 4F**), which increases after the first CCl_4 injection.
In summary, the spatiotemporal distribution patterns of the collagen network, aHSC, and Mph simulated by the DT align well with the experimental observations. The DT predicts that a gradient of DAMPs derived from CYP2E1-expressing cells determines the localization of ECM deposition around and between the closest CVs.

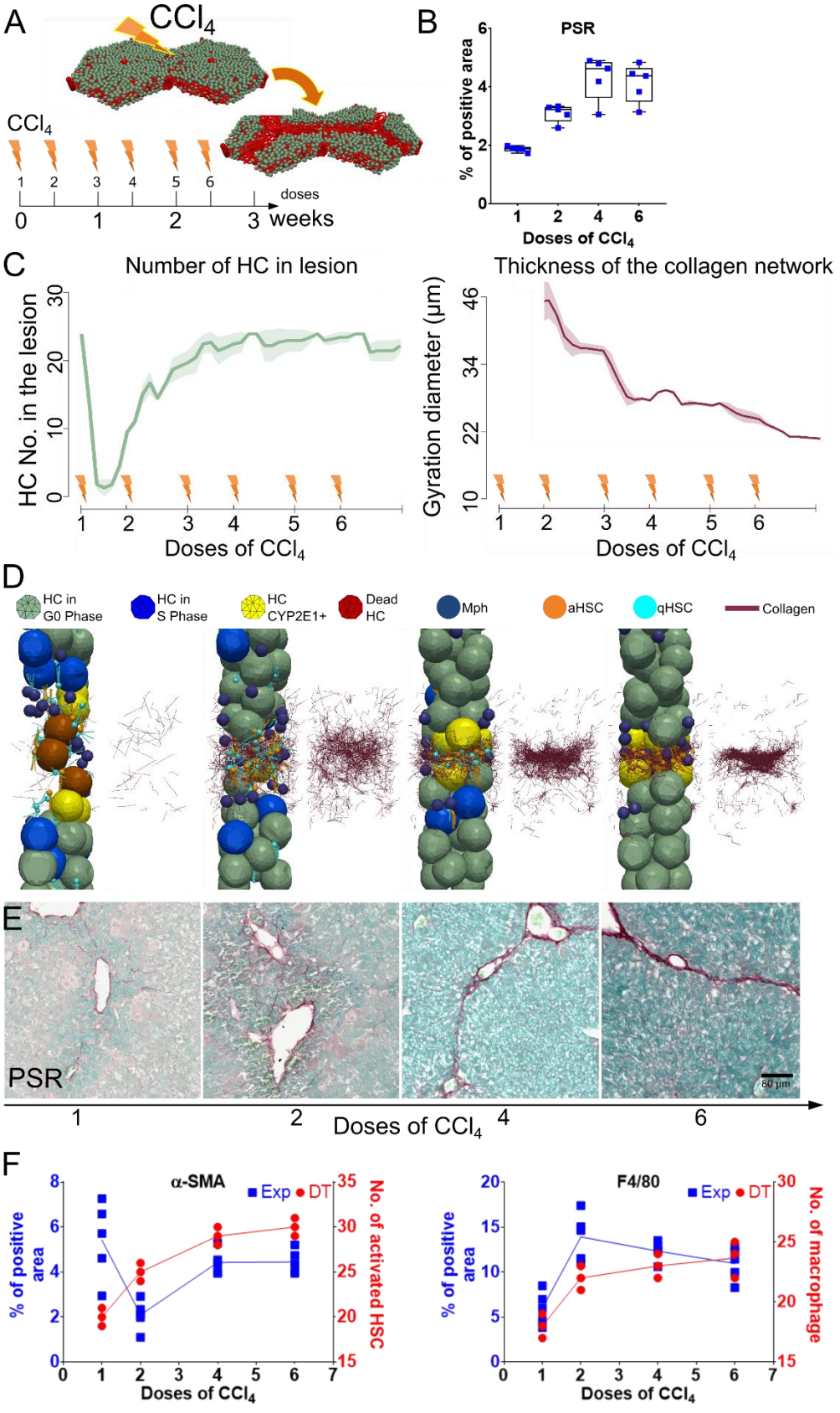
A
CCl4
CCl4
1 2 3 4 5 6
doses
0 1 2 3 weeks
B
PSR
% of positive area
0 2 4 6
1 2 4 6
Doses of CCl4
C
Number of HC in lesion
HC No. in the lesion
0 10 20 30
1 2 3 4 5 6
Doses of CCl4
Thickness of the collagen network
Gyration diameter (µm)
10 22 34 46
1 2 3 4 5 6
Doses of CCl4
D
HC in G0 Phase
HC in S Phase
HC CYP2E1+
Dead HC
Mph
aHSC
qHSC
Collagen
E
PSR
80 µm
1 2 4 6
Doses of CCl4
F
α-SMA
Exp DT
% of positive area
No. of activated HSC
0 2 4 6 8
15 20 25 30 35
0 1 2 3 4 5 6 7
Doses of CCl4
F4/80
Exp DT
% of positive area
No. of macrophage
0 5 10 15 20
15 20 25 30
0 1 2 3 4 5 6 7
Doses of CCl4

Figure 4. **DT reference simulation predicts formation of wall-pattern of liver fibrosis upon repetitive doses of CCl_4.** (A) We ran the simulation of repetitive doses of CCl_4 on the DT two-lobule system for 3 biological weeks. (B) The experimentally determined PSR positive area, resulting from different doses of CCl_4, as indicated. (C) Number of hepatocytes (HC) in the lesion and thickness of the collagen network over time. Thickness is measured by the gyration diameter of the ECM network. The error bar depicts the standard deviation of three independent simulations. (D) Snapshot of DT components (in the striped regions as shown in Fig. 1E; **Supplementary Movie 2**). (E) PSR staining of collagen fibres in the fibrotic mouse liver at repeated doses of CCl_4, as indicated (see details in Materials and Methods section, scale bars are 80μm). (F) Quantification of α-SMA and F4/80 positive areas, and the numbers of aHSCs and Mphs in the lesion as predicted from the DT. Experimental data are shown as the means ± SD of 5 mice per group.

(IV) Spatial distribution of cells expressing CYP2E1 drives ECM deposition through the release of DAMPs, while the division of hepatocytes shapes the resulting pattern of ECM deposition.

In order to elucidate the origin of the observed patterns in ECM deposition, cells expressing CYP2E1 were pinpointed as the source of DAMPs, both temporally and spatially. In cases of acute liver injury induced by CCl_4, the proportion of CV connected by CYP2E1-expressing hepatocytes increased from day 3 to average 2 connections per CV and remained constant until at least day 16 (**Fig. 2C, Supplementary Fig. 2B**). Surprisingly, in chronic liver injury, the majority of CVs display 3-4 connections with CYP2E1+ hepatocytes after 6 doses), which is 3-4 connections more than 3 days after the first injection (**Supplementary Fig. 6D**, and 2 connections more than >4days after the first injection (Fig. 2C). The identified pattern of CYP2E1+ cells was integrated into the DT as a source of DAMPs for subsequent CCl_4 injections (**Supplementary Fig. 2B and 7A**). Within this framework, the model predicts that spatial DAMPs lead to ECM deposition by attracting aHSC and Mph (**Supplementary Fig. 2A, 3A and B, 6B, Supplementary Movie 3**).

To test whether the spatial distribution of dying/damaged/stressed hepatocytes influences the shape of the observed collagen network, we conducted perturbation simulations. For instance, we considered a scenario with randomly distributed CYP2E1+ hepatocytes after the second CCl_4 injection (**Perturbation 1; P1, Fig. 5A**), as compared to the reference case, where CYP2E1-expressing hepatocytes were confined to the lesion. In this case, the resulting collagen network had a larger diameter and a more homogeneous distribution of collagen fibers (without forming a wall pattern), unlike the reference case (**P1, Fig. 5B, C, Supplementary Movie 4**).
To experimentally validate the DT simulation for P1, mice with altered spatial and absolute expression of CYP2E1 were tested. This is achieved by deletion of GATA4 from the endothelial cell. In these mice, removal of the transcription factor GATA4 ($GATA4^{LSEC\text{-}KO}$) from endothelial cells (Winkler et al. 2021) results in reduced Wnt2 expression. Wnt2 is a well-known upstream regulator of CYP2E1 expression (Rocha et al. 2015). Therefore, these mice showed a reduction of CYP2E1 positive hepatocyte fraction due to reduction of Wnt2 expression from LSEC. (**Fig. 5D, E**). These mice underwent chronic CCl_4 intoxication with 2 injections per week for 3 consecutive weeks. The resulting Cyp2E1+ hepatocyte pattern as known from the control mice was disrupted in chronic CCl_4-treated $GATA4^{LSEC\text{-}KO}$ mice, presenting with a more randomly distributed pattern (**Fig. 5F**). As predicted, the ECM deposition pattern was also compromised in 75% (6 out of 8) of the tested $GATA4^{LSEC\text{-}KO}$ mice, showing a more uniformly distributed perisinusoidal fibrosis, as compared to control mice displaying the septal pattern (**Fig. 5F**). This perturbation experiment suggests that the spatial distribution of CYP2E1+ cells is responsible for the septal fibrosis patterns that develop in the mouse liver due to chronic CCl_4 injections.

We also conducted *in silico* perturbations targeting hepatocyte proliferation, HSC activation, and Mph phagocytic activity, comparing the outcomes with the reference DT model (**Fig. 5A**). To assess the impact of biomechanical pressure from dividing hepatocytes on collagen organization, we ran the DT simulation by excluding hepatocyte proliferation for 21 days **(P2**). The model predicted that fewer hepatocytes would be present in the lesion compared to the reference model. Interestingly, the same amount of deposited ECM in the injured regions failed to form a fibrotic wall, as observed in the reference model after 6 doses of CCl_4. The collagen network diameter was much larger compared to the reference case (**P2; Fig. 5B, C, Supplementary Movie 5**). The relationship suggesting that fewer hepatocytes lead to a wider ECM network supports the conclusion that hepatocyte division is a significant driver of the experimentally observed septal fibrosis pattern, likely through biomechanically displacing and compressing the ECM fibres, which is absent in absence of hepatocyte proliferation (**Supplementary Fig. 9B, C**).

In another scenario, we investigated the influence of HSC phenotypes and activities on fibrosis pattern development and shaping. We conducted three independent perturbations. In the reference model, 50% of aHSC underwent apoptosis while 50% reverted to a quiescent state during regeneration (as determined in previous experimental studies; **Kisseleva et al. 2012**). In one perturbation, we assumed that 70% of aHSC became apoptotic (**P3**). In a second perturbation, aHSC migration was set to 0% (**P4**), and in a third perturbation, 100% of aHSC converted to a quiescent phenotype (**P5**). These perturbations were simulated with the DT for 3 weeks, involving 6 CCl_4 injections. In **P3**, the total number of deposited collagen fibers was significantly reduced, because 70% of aHSCs were lost after each round of CCl_4 injection, resulting in 40% fewer aHSCs in the perturbation model compared to the reference model, thus leading to less collagen deposition (**P3, Supplementary Fig. 10; Supplementary Movie 6**). In **P4**, there were fewer collagen fibers distributed along the lesion boundary, because HSC lacking migratory activity remained in their original position (**P4, Supplementary Fig. 10; Supplementary Movie 7**).

As a consequence, fewer HSC accumulated in the center of the lesion compared to the reference. In **P5**, collagen fiber deposition begins earlier compared to the reference model, around day 1.5 versus day 3 (**Fig. 5B**). This occurred because reverted HSCs are more responsive to DAMP-mediated activation. Perturbations **P3** and **P4** result in a compromised ECM deposition pattern, whereas **P5** leads to the same dense fibrotic wall in the center of the lesion after 6 CCl_4 injections. Although collagen fibers are generated earlier as compared to the reference, they are scattered within the lesion. The wall structure did not form earlier. This is evident in the gyration radii, where those of **P3** and **P4** are much larger, whereas that of **P5** is very similar to the reference model. The HSC-directed perturbations did not noticeably affect the number of hepatocytes in the lesion (**Fig. 5B, Supplementary Movie 8**). In summary, the HSC-directed model perturbations suggest that the HSC phenotype primarily impacts the absolute amount of ECM deposition, while HSC migration is crucial for the formation of the septal fibrosis pattern.

Finally, we assessed the phagocytic and migratory effects of Mph and conducted two separate Mph related perturbations with the DT. Mph transitioned to being Ly6C^{low} after 5 days following each CCl_4 injection, instead of the 12 hours as evident in the reference model (**P6**), or they were assumed to be deficient in migration ability (**P7; Fig. 5A**). Simulation P6 results in increased collagen fiber presence in the injured regions without altering the wall structure formation pattern (**Fig. 5C; Supplementary Movie 9**). Simulating Mph migration deficiency (**P7**) leads to the formation of a looser and more broadly distributed collagen fiber network (**Fig. 5A, Supplementary Movie 10**). Furthermore, the amount of deposited collagen increases, because the number of Mphs available in the lesion to degrade collagen fibers decreases (**Supplementary Fig. 10**). The gyration radius of the collagen network in simulations **P6** and **P7** is slightly larger than that in the reference model (**Fig. 5**). Perturbations **P6** and **P7** have no impact on the number of hepatocytes in the lesion (**Fig. 5B**). The perturbation results indicate that Mph activity has a minor effect on the development of the septal fibrosis pattern.

In conclusion, we propose that the septal fibrosis pattern observed in CCl_4-induced chronic liver disease in mice is primarily driven by the spatial distribution of CYP2E1+ hepatocytes, HSC activation and migration, and is shaped by mechanical pressure resulting from dividing hepatocytes.

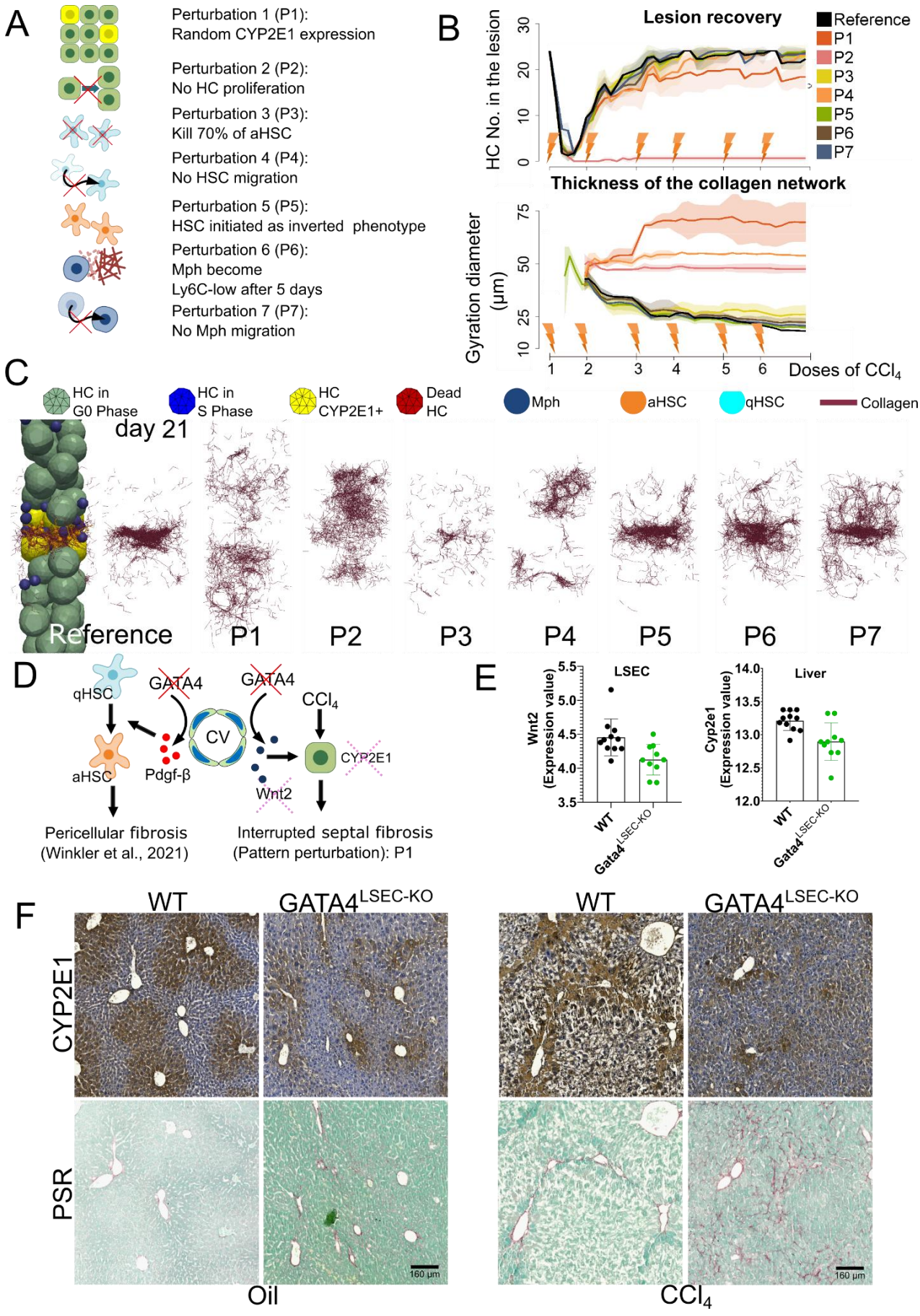
A
Perturbation 1 (P1):
Random CYP2E1 expression
Perturbation 2 (P2):
No HC proliferation
Perturbation 3 (P3):
Kill 70% of aHSC
Perturbation 4 (P4):
No HSC migration
Perturbation 5 (P5):
HSC initiated as inverted phenotype
Perturbation 6 (P6):
Mph become
Ly6C-low after 5 days
Perturbation 7 (P7):
No Mph migration
B
Lesion recovery
HC No. in the lesion
Reference
P1
P2
P3
P4
P5
P6
P7
Thickness of the collagen network
Gyration diameter (μm)
Doses of CCl4
C
HC in G0 Phase
HC in S Phase
HC CYP2E1+
Dead HC
Mph
aHSC
qHSC
Collagen
day 21
Reference
P1
P2
P3
P4
P5
P6
P7
D
qHSC
GATA4
GATA4
CCl4
CV
aHSC
Pdgf-β
CYP2E1
Wnt2
Pericellular fibrosis
(Winkler et al., 2021)
Interrupted septal fibrosis
(Pattern perturbation): P1
E
LSEC
Wnt2 (Expression value)
WT
Gata4LSEC-KO
Liver
Cyp2e1 (Expression value)
WT
Gata4LSEC-KO
F
WT
GATA4LSEC-KO
WT
GATA4LSEC-KO
CYP2E1
PSR
160 μm
160 μm
Oil
CCl4

Figure 5. **Perturbation simulations of DT components and experimental validation of predictions.** (A) Seven different perturbation scenarios were tested. P1, randomly distributed CYP2E1 expressing hepatocytes; P2, no hepatocyte proliferation; P3, 70% of activated HSCs undergo cell death; P4, HSCs do not migrate; P5, HSCs display an inverted phenotype after CCl4 injections; P6, macrophages become $Ly6C^{low}$, 5 days after CCl4 injections, and P7, macrophages cannot migrate. (B) Number of hepatocytes in the lesion and thickness of the collagen network during 3 weeks of chronic CCl4 injections. Thickness was determined by the gyration diameter of the network. The error bars represent the standard deviation of 3 simulation runs. (C) Snapshots of the collagen fibre network, resulting from the different perturbations, after 6 CCl_4 injections each (highlighted is the section as shown in **Fig. 1E**). (The corresponding time-course simulations are shown in Supplementary Movies 4-10). (D) Endothelial cell specific deletion of the transcription factor GATA4 (Winkler et al. 2021) leads to decreased availability of the WNT2 ligand and a disturbed pattern of CYP2E1+ hepatocytes. The model was used to experimentally validate perturbation scenario 1 (random CYP2E1 expression). (E) mRNA expression data (GSE141004) in endothelial cells isolated from $GATA4^{LSEC\text{-}KO}$ mice, showing downregulation of WNT2. (F) CYP2E1 and PSR staining of wild type (WT) and $GATA4^{LSEC\text{-}KO}$ mouse livers after 6 CCl_4 injections. Data are shown as the means ± SD of 6-8 mice per group.

Discussion

Liver fibrosis is characterized by the accumulation of ECM, in the here considered model linking the CVs of neighboring lobules by fibrotic walls due to injuries by repeated injections of CCl_4. A fundamental concept in understanding liver fibrosis is comprehending why and where ECM is deposited in specific patterns that eventually progress to cirrhotic nodules. However, a comprehensive grasp of this pattern formation has been impeded by its intricate complexity involving numerous components and subprocesses. This complexity makes it challenging to simultaneously monitor all aspects through experimentation.

In an effort to provide an alternative to a solely experimental approach, we have devised a digital twin (DT) of a two-lobule liver system. This model represents the fundamental tissue unit for the fibrosis pattern we have investigated. It relies on quantifiable experimental parameters to explore the potential sequence and interplay of subprocesses in the formation of fibrotic walls. The iterative process involves refining the model based on experimental guidance, making predictions, and validating the model through experimentation.

The DT encompasses a minimal selection of critical liver cell types (hepatocytes, hepatic stellate cells, and macrophages) as well as tissue elements (sinusoidal networks and collagen fibers). It serves as a platform to study the development, progression, and pattern formation of septal fibrosis following exposure to CCl_4. The DT further elucidates how mechanical interactions and molecular crosstalk between these tissue constituents contribute to the observed septal fibrosis pattern in experiments. To achieve this, the DT meticulously captures the temporal and spatial dynamics of tissue microarchitecture. It directly models cells and the ECM fiber network at a subcellular level of resolution, emulating their rearrangements and remodeling in response to repetitive CCl_4 exposure. At the current stage of the DT model, the intricate intracellular mechanisms governing cellular decisions and cell-cell communication have not been explicitly incorporated yet and are planned as follow up steps in the context of integrating models at molecular and cellular scales.

A simulation can be likened to studying a process in a well-defined setting under a microscope, similar as in live imaging, the latter, however, due to the duration of the process currently being out of reach. Repetitive exposure to CCl_4 leads to iterations of tissue damage caused by the demise of CYP2E1-positive hepatocytes, followed by incomplete regeneration through the division of surviving hepatocytes. In the DT model, the region of CYP2E1 positivity was determined based on experimental evidence linking adjacent CV from the second injection of CCl_4 onward.

The dynamic process of growing and dividing hepatocytes was stochastically sampled from the spatiotemporal distribution of Ki-67-positive hepatocytes surrounding the lesion over time. Migration of HSC and Mph was modeled by applying a constant force to the cells in the direction towards the gradient of DAMPs, as described in studies by Seo et al. (2013) and Roohani and Tacke (2021). Although the model could potentially be improved by incorporating cell protrusion anchorage in the ECM (Ribeiro et. al., 2016), it was deemed unnecessary, since we do not expect any change of the dynamics for the present study's objectives in the DT simulation.

DAMPs are emitted by damaged hepatocytes. After the initial exposure to CCl_4, the DAMPs concentrate around CVs. However, during subsequent regeneration phases, observations aligned with previous research (Ghafoory et al., 2013; Ghallab et al., 2019) showing that CYP2E1-expressing cells recover and form a wedge shape connecting CVs. Analyzing connected CVs through CYP2E1-expressing hepatocytes revealed that shortly after fibrosis establishment, one CV is linked to 3-4 neighboring CVs. This may occur if a CV collecting blood from one lobule splits into two CVs that are then associated with two (new) lobules: before branching, there is one circular CYP2E1-positive area surrounding the CV, which, after the CV branches into two CVs that are each associated with one of the two new lobules, remain connected until the two CVs are sufficiently far apart from each other (the branching concept is explained in **Fig. 3 and 4** in **Teutsch 2005**). Consequently, hepatocytes perish along these CV-CV connections after subsequent CCl_4 doses, altering the spatial pattern of DAMP sources from around the CV after the first dose to along the CV-CV connection in later doses. Thus, the time point of the second dose, 3 days after the initial CCl_4 exposure, was chosen as the model's initial reference point, encompassing critical fibrogenic factors such as the earliest signs of metabolic activity of midzonal hepatocytes (CYP2E1 expression), pronounced cell division, maximal HSC activation, and Mph infiltration. Most model parameters were calibrated based on data at this specific time point. Using the calibrated DT, simulations encompassing 6 consecutive CCl_4 injections were performed, with results being compared to experimental outcomes.

The DT simulations accurately replicated the experimentally observed scenario including the exact fibrosis wall pattern formation, suggesting that the spatial distribution of CYP2E1-expressing cells drives pattern formation through DAMP gradients originating from deceased hepatocytes. To test this concept, a mathematical analysis using the DT was conducted, considering a homogeneous distribution of CYP2E1-expressing cells. In such a scenario, the DT predicted dispersed DAMP concentrations resulting in homogeneous ECM deposition, as opposed to forming a linear wall as seen in the reference case. This hypothesis was examined using mice with partially disturbed CYP2E1-expression ($GATA4^{LSEC\text{-}KO}$), where the GATA4 transcription factor plays a role in LSEC specification and differentiation. These mice exhibit a more scattered CYP2E1 distribution, as compared to the control and administering repeated CCl_4 doses, similar to the model's setup, leads to a more scattered fibrosis pattern devoid of the expected formation, thereby validating the DT's prediction. This indicates that the spatial distribution of deceased hepatocytes, the source of DAMPs in chronic liver injury, significantly influences the overall fibrotic pattern.

While the pattern of CYP2E1+ hepatocytes shape the fibrosis's spatial arrangement, it does not elucidate the reason behind the sharp localization of fibrotic walls in the middle of the CYP2E1-positive region. The DT proposed that this phenomenon results from successive waves of hepatocyte

proliferation after repeated CCl_4 administrations. When the dead cell lesion closes, proliferating hepatocytes near the lesion mechanically displace ECM towards the center of the dead cell zone due to mechanical pressure. This prediction is supported by the observation that initially, ECM is scattered within the CYP2E1+ zone where aHSCs deposit it. Over time, the ECM becomes increasingly localized.

The intricate network structure and ECM density could not be directly measured. The DT predicts an appropriate density of around 1.0 mg/mL to explain fibrotic wall formation, a value consistent with the study by Stein et al. (2008). Different scenarios for the architecture of collagen networks were compared, with the scenario where collagen initially forms individual fibers that gradually crosslink fitting the observed collagen deposition pattern well. This configuration was selected for all subsequent DT simulations. Another DT prediction indicates that if a sufficient number of aHSC (20% more than in the reference case) are depleted, after each CCl_4 injection, the wall-shaped collagen network would not form due to the reduced number of collagen fibers. This aligns with prior experimental research demonstrating that the loss of aHSC leads to diminished fibrogenesis and matrix accumulation (Wu et al., 2017).

In addition to the overall global fibrosis pattern, surprisingly, the model managed to reproduce the local "chicken wire" pattern of collagen fibers observed at early stage of CCl_4-induced fibrosis, and as characteristic of steatotic and alcohol related liver disease. This was because aHSCs are generating collagen fibers while the remains of dead hepatocytes are still present, resulting in the fibers enveloping the dead bodies and forming scaffolds with large spaces. This further suggests the model's flexibility for other disease etiologies and confirms its clinical relevance.

In summary, the presented DT model effectively explains the formation of fibrotic walls in septal fibrosis. While other studies have addressed aspects of fibrosis formation, they often overlooked tissue microarchitecture or the influence of mechanical aspects.
Friedman and Hao (2017) developed a mathematical model aimed at investigating liver fibrosis by representing interactions among various cells and cytokines. However, their model utilized a "continuum" approach that involves averaging over multiple cell diameters, thus lacking the capability to capture tissue microarchitecture. Additionally, their focus was primarily on cell and molecular kinetics, omitting mechanical aspects. On the other hand, Dutta-Moscato et al. (2014) adopted an agent-based model that positioned cells on a two-dimensional fixed lattice. Unfortunately, this choice limited their ability to model cell and tissue biomechanics, which, as evidenced by the present DT emerged as a critical factor in fibrotic wall formation. Their work described the formation of fibrotic streaks along the portal field, which did not align with the potential of CYP2E1-positive hepatocytes driving such a process. In contrast, our research demonstrates that fibrotic walls are formed between CV, as indicated by experiments.
We firmly believe that the present mathematical model for septal fibrosis signifies a significant stride in developing a comprehensive liver DT for CLD. It serves as the starting point for extending the DT to encompass various etiologies, including biliary fibrosis. Additionally, the gradual integration of more cell types and processes into the model could enable us to simulate the progression towards non-compensated cirrhosis and hepatocellular carcinoma, which represent critical endpoints of CLD that go beyond the fibrosis stage.
The liver DT technology offers a multitude of opportunities. As demonstrated and noted by Drasdo and Zhao (2023), it can guide the selection and design of experiments. It facilitates testing the interplay of numerous mechanisms at different levels within a strictly defined computer-based environment, spanning from intracellular pathways to tissue and even whole-body levels, as shown by Dichamp et al. (2023). Similarly, as highlighted in the study addressing paracetamol (acetaminophen) toxicity by Hoehme et al. (2023), the present DT has the capacity to extrapolate outcomes from *in vitro* experiments to expected *in vivo* systems behavior, even across different species.
Although the application of the DT has been demonstrated with non-human data, its prospective implementation in human contexts has the potential to bridge the gap between human tissue cultures, bioengineered experiments, animal disease models and patient-related scenarios. While there might be initial setbacks, these failures can help identify and address critical knowledge gaps concerning mechanisms and parameters, ultimately contributing to a holistic comprehension of human liver disease.
Personalizing the DT for specific patients remains a major challenge. In addition to *in vivo* extrapolations from *in vitro* systems, which can involve data that are generated in cells extracted from a patient, or translating mouse data to human disease phenotypes, the DT can be of direct use in clinical settings. Integrating molecules determined at various disease stages that qualify as biomarkers, and using them as indicators, such as in histopathology, could complement evolving high-resolution technologies like high-magnetic field MRI or temporal diffusion spectroscopy.

While artificial intelligence (AI) approaches have their merits, mechanistic DTs offer predictive capabilities for unknown interventions and provide causal chains that elucidate underlying mechanisms for which no data is available. AI and mechanistic approaches can be complementary, with AI potentially informing mechanistic DTs and accelerating their development.

In conclusion, our presented DT offers a valuable framework for understanding fibrotic wall formation in septal fibrosis. This model constitutes a significant advancement in liver disease research and sets the stage for broader applications, bridging experimental and clinical domains and promoting a comprehensive understanding of chronic liver disease.

Limitation

Macrophages produce matrix metalloproteinases (MMPs) to digest the collagen fibres, they contribute to the survival of hepatic stellate cells (Duffield et al., 2005; Pradere et al., 2013), and they phagocytize dead cells (**Ramachandran et al., 2012**) . We here focussed on the phagocytizing function of macrophages only and did not consider a survival signal to aHSC provided by macrophages or other immune cells. In our DT, aHSC autonomously does not revert or die before either the lesion is closed, or a certain collagen density is locally reached. As a consequence, depletion of macrophages in the DT did not shorten lifetime of aHSC but only reduced the degradation of the collagen network. Such further refinements will be addressed in future versions of the DT along with further applications in disease progression, as e.g. until HCC.

Supplementary Information

Methods

Assessment of liver transaminases. Blood was collected in Li-Heparin vials from the retrobulbar plexus and centrifuged at 13,000 rpm at 4°C for 6

min. Plasma was subsequently stored at −80°C until further analysis. Then, alanine aminotransferase (ALT), and aspartate aminotransferase (AST) were measured using a Hitachi automatic analyzer (Core facility-Medical Faculty Mannheim, Germany).

RNA isolation and quantitative real-time (RT)-PCR. RNA from liver tissues was isolated using the InviTrap spin kit according to the manufacturer's instructions. Liver tissues from the mice were cut into approximately 20 mg, and were homogenized with a Precellys Evolution machine two times (20 s, 5 s pulse, 2s break), then the supernatants were collected. Then, 300 µL β-mercaptoethanol-containing lysis solution TR were immediately added to each sample. The resulting lysate was directly pipetted onto the DNA-Binding Spin Filter which was placed in a 2 mL Receiver Tube. Samples were incubated for 1 min at room temperature and were centrifuged at 11000 rpm for 2 min. After discarding the DNA-Binding Spin Filter, 250 µL of 70% ethanol were added to each tube and were completely mixed with the lysates. The mixtures were transferred to RNA-RTA Spin Filters, and were incubated for 1 min. Samples were centrifuged at 11000 rpm for 1 min. Then 600 µL of Wash Buffer R1 were added into the RNA-RTA Spin Filter after discarding the flow-through, then this mixture was centrifuged for 1 min at 11000 rpm. After discarding the flow-through, 700 µL of Wash Buffer R2 were added into the Filter, the same centrifuge step was performed as a wash step using buffer R1. The R2 washing step was repeated once. To eliminate any trace of ethanol in the RNA-RTA Spin Filter membrane, the tubes were centrifuged for 4 min at maximum speed. The RNA-RTA Spin Filters were transferred into RNase-free Elution Tubes and 30 µL of Elution Buffer R was pipetted. After 2 min incubation and 1 min centrifugation at 11000rpm, total RNA was collected, and transferred immediately on ice. The concentration was photometrically determined by measuring the RNA solution in a nanocrystalline plate at 260 nm with a Tecan infinite M200.From 1 µg total RNA, cDNA was transcribed with RevertAid H Minus Reverse Transcriptase (Thermo Fischer Scientific, USA, cat. no. EP0451) and used for RT-PCR with PowerUP SYBR Green Master Mix (Life Technologies, USA, cat. no. A25918) in a StepOnePlus RT-PCR System (Applied Biosystems USA from Thermo Fisher Scientific, Germany, cat. no. 4376600). A list of the primer pairs used (Eurofins, Germany) is provided in **Supplementary Table 1**. *Ppia* was theused as an internal reference gene. Target gene relative expression was determined with the ΔΔCt method, and a melt curve was created to ensure primer specificity. Each sample was measured in triplicate.

Supplementary table 1: Sequences of primer pairs used for real time PCR

Gene	Species	Forward	Reverse
Acta2 (α-Sma)	Mouse	TTCGCTGTCTACCTTCCAGC	GAGGCGCTGATCCACAAAAC
Timp1	Mouse	GGCATCTGGCATCCTCTTGT	ACTCTTCACTGCGGTTCTGG
Cd68	Mouse	GGCGGTGGAATACAATGTGTCC	AGCAGGTCAAGGTGAACAGCTG
Col1α1	Mouse	ACGTGGAAACCCGAGGTATG	TTGGGTCCCTCGACTCCTAC
Col1α2	Mouse	AGTCGATGGCTGCTCCAAAA	AGCACCACCAATGTCCAGAG

Cyp2e1	Mouse	CGTTGCCTTGCTTGTCTGGA	AAGAAAGGAATTGGGAAAGGTCC
Desmin	Mouse	TACACCTGCGAGATTGATGC	ACATCCAAGGCCATCTTCAC
Mmp9	Mouse	GCAGAGGCATACTTGTACCG	TGATGTTATGATGGTCCCACTTG
Ppia	Mouse	GAGCTGTTTGCAGACAAAGTC	CCCTGGCACATGAATCCTGG
Tgfβ1	Mouse	AGGGCTACCATGCCAACTTC	CCACGTAGTAGACGATGGGC

Spatial distribution of proliferating hepatocytes and aHSC

The detection of the dividing cells nuclei (Fig. 2F) was obtained by a global thresholding on the Hue and Saturation channels of the images. A post-processing step was applied to remove too small and large connected components considered as artifacts. Furthermore, touching nuclei were separated using the morphological watershed algorithm. The segmentation function was the euclidean distance transform on the binary image of the nuclei and the markers were obtained by computing the extended minima transform on the euclidean transform image. These different morphological operations are standard in image analysis and further details can be found in (**Soille 1999**). A final post-processing based on a shape criteria, i.e. the eccentricity, is performed: objects with an eccentricity less than 0.9 are removed.

The stained histological images of HSC are first binarized using local Otsu thresholding to obtain the whole fibrotic pattern. In order to individualize the fibrotic streets, the fibrotic region around each central vein is computed using the so-called *rolling ball algorithm* (**Sternberg 1986**): a disk of iteratively increasing radius *r* is rolling over the central vein boundary until the area ratio of HSC reaches a certain threshold ($\leq$ *0.8* in practice). The maximal radius □□□□,□ returned by the algorithm defines the width of the fibrotic region around the central vein labeled □ , a region which is called the *central fibrotic region* (**Supplementary Fig. 4A**, here the green circles do not cover all brown stainings around CV, which is not needed as our purpose is not to quantify the precise width of the brownish region around the CV, but to identify the fibrotic region between the CVs and quantify it. For this an accurate segmentation of the brown stainings around the CV is not required). An individual fibrotic street is therefore defined as the fibrotic pattern linking two neighboring central fibrotic regions. The second main step is the computation of the envelope image of each fibrotic street using i) a morphological closing operation on the binary image of the street to smooth its contour, and ii) an operation to fill the holes within the street. The envelope image is the resulting binary image after these two operations (see **Supplementary Fig. 4**). The third and final step before quantifying the width distribution of the fibrotic streets is the rotation of each envelope image to align their main axis with the y-axis (see **Supplementary Fig. 4**). Consequently, the width distribution of a given street is defined as the length distribution of the intersections between an horizontal line and the envelope image, the horizontal line being translated in the y-direction. To remove noise in the computation of these lengths, a moving average technique is used. The final results are presented in **Supplementary Fig. 4** as the concatenation of all width distributions of the fibrotic streets for the three mice M1, M2 and M3. In order to check whether or not there is a significant difference between widths computed close central veins and the ones further away, the width distributions are presented with respect to the normalized distance to its closest central vein, hence encompassing the spatial nature of the fibrotic street formation (the maximal distance being in the middle of the given fibrotic street). The results do not show any strong dependency of the fibrotic street width with respect to the central vein distance.

The computation of the spatial distribution of the dividing cell was performed using a kernel density estimator method. In practise, a non-parametric kernel density estimation is used, i.e. the probability that a nuclei of a dividing cell belongs to the position $x \in R^2$ is given by:

$$f(x) = \sum_{i=1}^{n} \frac{1}{nh^2} k(\frac{||x-x_i||}{h}),$$

where k is a symmetric kernel function (typically a Gaussian kernel is used here), n is the total number of nuclei segmented and x_i is the centroid location of nuclei i.

The polygonal contours of the necrotic regions are drawn on the image by a biologist expert using Image J. The mask image of the necrotic region is obtained and a morphological closing using a small size structuring element is performed to get smoother contours for the necrotic regions.

Mathematical physical modeling. To capture the approximate shape of cells and elements (e.g. sinusoids and collagen fibres), they are represented as individual objects with different geometric shapes. Hepatocytes close to the lesion are represented by triangulated structure consisting of discretized nodes connected by viscoelastic elements (DCM model, **Van Liedekerke et al. 2020**); hepatocytes far away from the lesion are represented by homogeneous isotropic elastic adhesive spheres; macrophages are represented by homogeneous isotropic elastic adhesive spheres; an HSC is represented as a sphere forming the cell's core body, connected to four semi-flexible chains of spheres; sinusoids are represented as chains of homogeneous isotropic elastic spheres; collagen fibres are represented as elastic springs that can resist stretching and bending.

Equation of motion for CBM-based hepatocytes. Each CBM (center-based model)-based hepatocyte is represented as a homogeneous isotropic, elastic, adhesive sphere. It can migrate, grow, divide, and interact with other cells or elements. The position of hepatocyte i is updated from:

$$\Gamma_{env,i}\vec{v}_i + \sum_j \Gamma_{i,j}(\vec{v}_i - \vec{v}_j) = \sum_j \vec{F}_{ij} + \vec{F}_{mig,i}, \qquad (1)$$

where $\Gamma_{env,i}$ is the friction coefficient with the environment, $\Gamma_{i,j} = \gamma_{\perp}(\vec{e}_{ij}\otimes\vec{e}_{ij}) + \gamma_{\parallel}(I - \vec{e}_{ij}\otimes\vec{e}_{ij})$ is the friction tensor between cell i and sphere j, and $\vec{e}_{ij}$ is the unit vector from i towards j, $\vec{F}_{ij}$ is the corresponding central repulsion/adhesion interaction force, $\vec{F}_{mig,i}$ is an (active) migration force of cell i. The central force is computed by **(Popov 2010**):

$$\vec{F}_{ij} = (\frac{4\hat{E}}{3\hat{R}}[a(\delta_{ij})]^3 - \sqrt{8\pi\sigma\hat{E}[a(\delta_{ij})]^3})\vec{e}_{ij}, \qquad (2)$$

where the contact radius $a(\delta_{ij})$ allows to compute hepatocyte-hepatocyte contact area, and can be obtained by $\delta_{ij} = \frac{a^2}{\hat{R}} - \sqrt{\frac{2\pi\sigma}{\hat{E}}}$, $\hat{E}$ and $\hat{R}$ are defined as $\hat{E} = (\frac{1-\nu_i^2}{E_i} + \frac{1-\nu_j^2}{E_j})^{-1}$ and $\hat{R} = (\frac{1}{r_i} + \frac{1}{r_j})^{-1}$, with E_i and E_j being the Young's moduli, ν_i and ν_j the Poisson ratios, and r_i and r_j the radii of i and j. The migration force is computed by $\vec{F}_{mig,i} = f_{dir}\vec{e}_i + \sqrt{6D_i/\Delta t}\vec{r}_i$, where f_{dir} is one constant force magnitude, $\vec{e}_i$ is the unit vector from i towards the central vein, D_i is the diffusion constant of i, $\vec{r}_i$ is one random unit vector, Δt is the time step of our simulation (**Hoehme et al. 2010**).

Equation of motion for DCM-based hepatocytes. Each DCM (deformable cell model)-based hepatocyte is modeled as a triangulated structure consisting of discretized nodes connected by viscoelastic elements. For one hepatocyte, the position of each i of its node is updated by solving the following equation of motion:

$$\Gamma_{env,i}\vec{v}_i + \sum_j \Gamma_{i,j}(\vec{v}_i - \vec{v}_j) = \sum_j \vec{F}_{e,ij} + \sum_m \vec{F}_{m,i} + \vec{F}_{vol,i} + \sum_T \vec{F}_{T,i} + \vec{F}_{rep,i} + \vec{F}_{adh,i}, \qquad (3)$$

where $\Gamma_{env,i}$ is the friction coefficient with the environment, $\Gamma_{i,j}$ is the friction tensor between i and other node j, $\vec{F}_{e,ij}$ is the in-plane elastic force with node j, $\vec{F}_{m,i}$ is the bending force with node m, $\vec{F}_{vol,i}$ is the volume force controlled by the cell compressibility, $\sum_T \vec{F}_{T,i}$ is the force that avoids excessive triangle distortion of triangle T which contains i, $\vec{F}_{rep,i}$ is the repulsion force on the local surface, $\vec{F}_{adh,i}$ is the adhesion force with nearby objects. The detailed expression of Eqn. (3) can be seen in **Van Liedekerke et al. 2020**.

Equation of motion for macrophages. Each macrophage is represented as a homogeneous isotropic, elastic, adhesive sphere. It can migrate and interact with other cells or elements. The position of macrophage i is updated by solving the following equation:

$$\Gamma_{env,i}\vec{v}_i + \sum_j \Gamma_{i,j}(\vec{v}_i - \vec{v}_j) = \sum_j \vec{F}_{ij} + \vec{F}_{mig,i}, \qquad (4)$$

where $\Gamma_{env,i}$ is the friction coefficient with the environment, $\Gamma_{i,j}$ is the friction tensor between i and j (same as Eqn. 1), $\vec{F}_{ij}$ is the corresponding central repulsion/adhesion interaction force, $\vec{F}_{mig,i}$ is the migration force to drive i to migrate.

Equation of motion for HSC. The core body of HSC is modeled as one homogeneous isotropic, elastic, adhesive sphere (mainly representing the

HSC's nucleus) with several semi-flexible chains of spheres as "arms" (to mimic the long HSC's protruding branches). The position of one HSC sphere i is updated by solving the following equation of motion:

$\Gamma_{env,i}\vec{v}_i + \sum_j \Gamma_{i,j}(\vec{v}_i - \vec{v}_j) = \sum_j \vec{F}_{ij} + \vec{F}_{mig,i} + \sum_k \vec{F}_{ela,ik}$, (5)

where $\Gamma_{env,i}$ is the friction coefficient with the environment, $\Gamma_{i,j}$ is the friction tensor between i and another cell or element j (same as Eqn. 1), $\vec{F}_{ij}$ is the interaction force between i and another cell or element j (same as Eqn. 2). $\vec{F}_{ela,ik}$ represents elastic force between the body center i and the connected spheres k of its arms. is the migration force to drive i to migrate. The equation of motion for a sphere representing element i of a HSC's arm is approximated by:

$\Gamma_{ECM,i}\vec{v}_i + \sum_j \Gamma_{i,j}(\vec{v}_i - \vec{v}_j) = \sum_j \vec{F}_{ij} + \sum_k \vec{F}_{ela,ik}$, (5b)

where j represents interacting cells or elements, and k the connected spheres belonging to the same HSC's arm as element i does.

Equation of motion for the sinusoid spheres. Sinusoids are modeled as semi-flexible spheres (**Hoehme et al. 2010**). For one sinusoid sphere i, the position of i is updated by solving the following equation of motion:

$\Gamma_{env,i}\vec{v}_i = \sum_j (\Gamma_{i,j}(\vec{v}_i - \vec{v}_j) + \vec{F}_{ij}) + \sum_k (\Gamma_{i,k}(\vec{w}_{ik} - \vec{e}_{ik}(\vec{w}_{ik} \cdot \vec{e}_{ik})) + \vec{F}_{ik})$, (6)

where $\Gamma_{env,i}$ is the friction coefficient with the environment, $\Gamma_{i,j}$ is the friction tensor between i and another cell j (same as Eqn. 1), $\vec{F}_{ij}$ is the interaction force between i and j (same as Eqn. 2), $\vec{w}_{ik} = \vec{w}_k - \vec{v}_i$ is the difference of velocity between i and another sinusoid sphere k, $\vec{e}_{ik}$ is the unit direction vector from i towards k, $\vec{F}_{ik}$ is the interaction force between i and k.

Modeling of collagen fibres

Network generation approach. In a given gel space Ω_g (volume of Ω_g is V_g), the total volume of the collagen fibre V_c is determined by $V_c = V_g \rho_c \upsilon_c$, where $\upsilon_c = 1.89\, ml/g$ is the specific volume of collagen (**Levick et al. 1987**), $\rho_c = 1.0\, mg/ml$ is the mass density of collagen (**Stein et al. 2008**). Then the total length of collagen fibre, L_{tot} deposited in the given space is given by $L_{tot} = V_c/\pi r_c^2$, where r_c is the radius of collagen fibre. The networks are grown one fibre at a time until the network achieves the total fibre length L_{tot}. (1) Insert a fibre i in Ω_g. It is assigned an initial point u_0^i and an initial tangent direction $\vec{\theta}_0^i$, both are chosen from a uniform distribution. A fibre length L_f is also assigned to i, where $< L_f > \sim 6\mu m$ (Stein et al., 2008). Grow the fibre after n extensions of segments in particular direction $\vec{\theta}_{j+1}^i = \vec{\theta}_j^i + \Delta\vec{\theta}_j^i, j = 0, \dots, n-1$ until L_f is reached. The length of each extended segment is $L_c = 3\ \mu m$ (**Stein et al. 2008**). Stop until the target total fibre length L_{tot} is reached, (2) Apply random force onto each of the fibres and update their positions. Crosslinks are added if any two fibre segments are closer than a distance threshold of 1.5 μm (**Supplementary Fig. 5A**). (3) Repeat step (2) until all fibres in Ω_g are connected into one network through crosslinks.

The elastic force and bending force on collagen fibre. Suppose the collagen fibre consists of several nodes and edges (**Supplementary Fig. 5B**). The elastic force at node x_n can be written as $\vec{f}_e(x_n) = k(\Delta l_{n-1}\frac{\vec{l}_{n-1}}{|\vec{l}_{n-1}|} + \Delta l_n \frac{\vec{l}_n}{|\vec{l}_n|})$, where k is the elasticity constant, Δl_n is the local displacement of edge $\vec{l}_n$.

Moreover, the bending energy at x_n can be written as $U(x_n) = \frac{1}{2}\int_{x_0}^{x_n} EI\kappa(s)^2 ds$, where E is the Young's modulus, I is the second moment of area, κ is the local curvature at x_n. Then the bending energy due to the bending angle θ_n at x_n can be approximated as:

$\Delta U(x_n) = U(x_n) - U(x_{n-1}) \approx \frac{1}{2} EI\kappa(x_n)^2 |l_n| \approx \frac{1}{2} EI(\theta_n - \theta_{n,0})^2/|l_n|$ (for $\kappa(x_n) \approx \theta_n/l_n$), where $\theta_{n,0}$ is a constant equilibrium angle for x_n. The bending force is evaluated by derivative of involved $\Delta U(x_{n+i})$ over x_n:

$\vec{f}_b(x_n) = \sum_{i=-1}^{1} \nabla_{x_n} \Delta U(x_{n+i}) = \sum_{i=-1}^{1} \frac{\partial \Delta U(x_{n+i})}{\partial cos(\theta_{n+i} - \theta_{n,0})} \nabla_{x_n} cos(\theta_{n+i} - \theta_{n,0})$, (7)

We denote $\vec{l}_n = \vec{x}_{n+1} - \vec{x}_n$ and $\vec{l}_{n-1} = \vec{x}_n - \vec{x}_{n-1}$, then we can get $cos\ cos(\theta_n - \theta_{n,0}) = \frac{(R_{\theta_1}\vec{l}_n)^T (R_{\theta_2}\vec{l}_{n-1})}{|l_n||l_{n-1}|}$, where R_{θ_1} and R_{θ_2} are two rotational matrices satisfying $\theta_1 - \theta_2 = \theta_{n,0}$. It is easy to get $R_{\theta_2}^T R_{\theta_1} = R_{\theta_1 - \theta_2} = R_{\theta_{n,0}}$, which is also a constant matrix. Then we have $\frac{\partial \Delta U(x_n)}{\partial cos(\theta_n - \theta_{n,0})} = -EI\frac{\theta_n - \theta_{n,0}}{sin(\theta_n - \theta_{n,0})}$. Using the property of vector calculus identities $\nabla(A \cdot B) = B \cdot (\nabla A) + A \cdot (\nabla B)$, we have:

$$\nabla_{x_n} cos(\square_n - \square_{n,0}) = \nabla_{x_n} \frac{\left(R_{\theta_1}\vec{l}_n\right)^T\left(R_{\theta_2}\vec{l}_{n-1}\right)}{|l_n||l_{n-1}|} = \frac{\nabla_{x_n}\left(\left(R_{\theta_1}\vec{l}_n\right)^T\left(R_{\theta_2}\vec{l}_{n-1}\right)\right)|l_n||l_{n-1}| - \left(R_{\theta_1}\vec{l}_n\right)^T\left(R_{\theta_2}\vec{l}_{n-1}\right)\nabla_{x_n}(|l_n||l_{n-1}|)}{|l_n|^2|l_{n-1}|^2} = \frac{R_{\theta_{n,0}}\vec{l}_n - R_{-\theta_{n,0}}\vec{l}_{n-1}}{|l_n||l_{n-1}|} + \frac{\vec{l}_n{}^T\left(R_{-\theta_{n,0}}\vec{l}_{n-1}\right)}{|l_n||l_{n-1}|}\left(\frac{\vec{l}_n}{|l_n|^2} - \frac{\vec{l}_{n-1}}{|l_{n-1}|^2}\right), \quad (8)$$

Accordingly, we also have

$$\nabla_{x_n} cos(\square_{n-1} - \square_{n,0}) = \frac{-1}{|l_{n-1}||l_{n-2}|}\left(\frac{\vec{l}_{n-1}{}^T R_{-\theta_{n,0}}\vec{l}_{n-2}}{|l_{n-1}|^2}\vec{l}_{n-1} - R_{-\theta_{n,0}}\vec{l}_{n-2}\right) \text{ and}$$

$$\nabla_{x_n} cos(\square_{n+1} - \square_{n,0}) = \frac{1}{|l_{n+1}||l_n|}\left(\frac{\vec{l}_{n+1}{}^T R_{-\theta_{n,0}}\vec{l}_n}{|l_n|^2}\vec{l}_n - R_{\theta_{n,0}}\vec{l}_{n+1}\right).$$

We denote $\nabla_{x_n} cos(\square_{n-1} - \square_{n,0})$ as a vector $\vec{d}_1(x_n)$, $\nabla_{x_n} cos(\square_n - \square_{n,0})$ as a vector $\vec{d}_2(x_n)$, and $\nabla_{x_n} cos(\square_{n+1} - \square_{n,0})$ as a vector $\vec{d}_3(x_n)$,. Thus, for each node x_n in the fibre, the bending force is obtained as:

$$\vec{f}_b(x_n) = \frac{-EI}{|l_{n-1}|}\frac{\theta_{n-1}-\theta_{n,0}}{sinsin\,(\theta_{n-1}-\theta_{n,0})}\vec{d}_1(x_n) + \frac{-EI}{|l_n|}\frac{\theta_n-\theta_{n,0}}{sinsin\,(\theta_n-\theta_{n,0})}\vec{d}_2(x_n) + \frac{-EI}{|l_{n+1}|}\frac{\theta_{n+1}-\theta_{n,0}}{sinsin\,(\theta_{n+1}-\theta_{n,0})}\vec{d}_3(x_n), \quad (9)$$

Equation of motion for collagen fibre nodes. The center of mass position of each collagen fibre node i is obtained by from an overdamped Langevin equation of motion, which summarizes all forces on i:

$$\Gamma_{c,i}\vec{v}_i + \sum_j \Gamma_{i,j}\left(\vec{v}_i - \vec{v}_j\right) = \sum_j \vec{F}_{c,el,ij} + \sum_j \vec{F}_{c,be,ij} + \sum_j \vec{F}_{cc,ij}, \quad (10)$$

where $\Gamma_{c,i} = \frac{1}{2}\sum_j \gamma_\perp^{c,j}\left(\vec{e}_{ij}\otimes\vec{e}_{ij}\right) + \gamma_\parallel^{c,j}\left(I - \vec{e}_{ij}\otimes\vec{e}_{ij}\right)$ is the collagen-environment friction tensor, $\vec{e}_{ij}$ is the unit orientation vector of fibre j connecting node i. $\gamma_\perp^{c,j}$ and $\gamma_\parallel^{c,j}$ are the perpendicular and parallel components of the friction of fibre j. $\gamma_\perp^{c,j}$ and $\gamma_\parallel^{c,j}$ can be approximated as $\gamma_\perp^{c,j} = 4\pi\eta_0 L_j/($ $ln\ ln\left(\frac{L_j}{2r_j}\right) + \rho_\perp)$ and $\gamma_\parallel^{c,j} = 2\pi\eta_0 L_j/(ln\ ln\left(\frac{L_j}{2r_j}\right) + \rho_\parallel$ (**Yang et al. 2017**), where L_j and r_j are the length and radius of fibre j. $\rho_\perp$ and $\rho_\parallel$ are two correction factors for approximating friction coefficient for rod-like objects (**Cox 1970**). $\Gamma_{\square,\square}$ is the friction tensor between the spring containing $\square$ and other cell or element $\square$ contacted with the spring (same as in Eqn. 3). The first term of right-hand side (rhs) of Eqn. (10) represents the elastic force exerted on i from elastic springs connecting i. The second term of rhs of Eqn. (10) represent the bending force exerted on i from bending springs connecting i. The third term of rhs of Eqn. (10) represent the interaction force between the spring containing i and other elements (e.g. hepatocytes or sinusoids).

Measurement of the height of the collagen network

The height of the collagen network was measured by the gyration radius in y-axis (the direction of pressure from other cells) of the collagen network by $r_{gyr} = \sqrt{\frac{1}{N}\sum_i \left(r_{i,y} - \frac{1}{N}\sum_j \quad r_{j,y}\right)^2}$, where $r_{i,y}$ is the y-coordinate of collagen node i.

Forces between cells and elements. The total force between cell/element i and cell/element j can be approximated by the sum of a repulsive and an adhesive force, which are characterized by a function of the geometrical overlap δ_{ij}. Since cellular adhesion force is due to the specific ligand-receptor on cell surface, we assume that there is only adhesive force between two hepatocytes, which can be approximated by Johnson-Kendal-Roberts (JKR) model following previous study (**Popov 2010**). For two hepatocytes i and j, the interaction force is computed using Eqn. (2). For the other cells and elements (e.g. collagen fibre), we use Hertz model to approximate the repulsive force between them (**Popov 2010**). For two spherical cell objects i and j, the Hertz repulsive force is computed by

$$\vec{F}_{rep,ij} = \frac{4\hat{E}}{3}\sqrt{\hat{R}}\delta_{ij}{}^{3/2}\frac{\vec{e}_{ij}}{|\vec{e}_{ij}|}, \quad (11)$$

where $\hat{E}$ and $\hat{R}$ are as defined in Eqn. (2). $\vec{e}_{ij}$ is the unit vector from i towards j.

For two collagen fibre springs i and j, the Hertz repulsive force is computed by

$$\vec{F}_{rep,ij} = \frac{4\hat{E}}{3}\sqrt{\hat{R}}\delta_{ij}{}^{3/2}\frac{\vec{e}_{ij}}{|\vec{e}_{ij}|}, \quad (12)$$

where r_i and r_j are the radii of springs i and j, respectively to calculate $\hat{R}$.

For one spherical cell object i and one collagen fibre j, the Hertz force repulsive force is computed by

$\vec{F}_{rep,ij} = \frac{2\hat{E}}{3}(\sqrt{\hat{R}} + \sqrt{r_i})\delta_{ij}{}^{3/2}\frac{\vec{e}_{ij}}{|\vec{e}_{ij}|}$, (13)

where r_j is the radius of the fibre spring j.

For one triangle of DCM-based hepatocyte i and fibre spring j, we applied the algorithm of triangle-cylinder collision detection (**Karabassi et al. 1999**) to check the collision type between i and j. If i and j contact with parallel axes, the Hertz force repulsive force is computed by

$\vec{F}_{rep,ij} = \frac{\pi}{4}\hat{E}L_{ij}\delta_{ij}\frac{\vec{e}_{ij}}{|\vec{e}_{ij}|}$, (14)

where L_{ij} is the length of the overlapped section between i and j (see **Karabassi et al. 1999** for the calculation of L_{ij}).

If i and j contact with non-parallel axes, the Hertz force repulsive force is computed by

$\vec{F}_{rep,ij} = 2\hat{E}r_j\delta_{ij}\frac{\vec{e}_{ij}}{|\vec{e}_{ij}|}$, (15)

where r_j is the radius of j.

Validation of the collagen model

We validated our collagen model by comparing two types of mechanical test on collagens with experimental data. We first applied the model to simulate the deformation of one single collagen fibre upon external force as depicted in (**Yang et al. 2008**). One fibre with length of 3μm consisting of 20 segments is fixed by the two ends. A force is applied perpendicularly on the fibre on three different positions (we assume y-axis is along the direction of the applied force, **Supplementary Fig. 5C**). The displacement of the fibre is calculated as the largest displacement of the fibre node on the y-axis. The simulated relationship between fibre displacement and magnitude of applied force can perfectly fit the experimental observation (**Supplementary Fig. 5D**).

We then applied the model to simulate the stress of the collagen network under compression (**Supplementary Fig. 5E**). A fibre network with size of 42.8×42.8×42.8 μm^3 is generated. The collagen nodes in the top layer (< 3 μm from the top) is fixed. The collagen network is compressed by pushing the nodes in the bottom layer (< 3 μm from the bottom) upwards (y-axis is along the up-bottom direction). The strain is calculated as $(\sum_{i\in top} y_i - \sum_{i\in bottom} y_i)/(\sum_{i\in top} y_{i,0} - \sum_{i\in bottom} y_{i,0})$, where y_i and $y_{i,0}$ are the y-coordinate and initial y-coordinate of collagen node i. We use two approaches to measure stress.

Approach one. Stress is calculated as $\sum_{i\in top} f_{y,i}/A$, where $f_{y,i}$ is the projection of force on the y-axis of collagen node i, $A = (x_{max} - x_{min}) \times (z_{max} - z_{min})$, x_{max}, x_{min}, z_{max} and z_{min} are the maximum and minimum x-coordinates and z-coordinates of all collagen nodes in the network, respectively.

Approach two. Stress tensor $\sigma = \frac{1}{V}\sum_{i>j}\vec{f}_{ij} \otimes \vec{e}_{ij}$, where $\vec{e}_{ij}$ is string vector between collagen nodes i and j, $\vec{f}_{ij}$ is the force exerted on $\vec{e}_{ij}$, V is the volume of the cubic space occupied by the network, that is 42.8×42.8×42.8 μm^3. Then the stress is taken as the y-element of the diagonal of σ (compression is along the y-axis).

The strain-stress curve of our simulation can fit the experimental data (**Ferruzzi et al. 2019**, **Supplementary Fig. 5G**).

Plasticity test of the collagen network. During the liver fibrosis process, HSCs produce collagen fibres while macrophages degrade collagen fibres simultaneously. The dynamic of production and degradation of collagen fibres might change the mechanical property of the collagen network (e.g. plasticity instead of elasticity). Here we did one plasticity test by rebuilding the collagen network we used for compression test (**Supplementary Fig. 5F**): (1) we compressed the collagen network to one degree of deformation; (2) we randomly removed some collagen fibres from the network (the removed number of fibres is calculated according to a given fraction, e.g. if the given fraction is 5%, then 5% of the fibres would be removed) and added the same number of new collagen fibres back; (3) the newly added collagen fibres were then crosslinked into the network; (4) we released the compressed network and measured the stress-strain curve and compared it with the curve from pure compression test. Such rebuilding process (removing and adding fibres) is to mimic the process that Mphs degrade while HSCs produce collagen fibres simultaneously during fibrosis progression. As shown in **Supplementary Fig. 5G**, after removing and adding new collagen fibres, the stress of the collagen network dropped significantly and it displayed plasticity (permanent deformation after stress reached to zero). The more collagen fibres were removed and added, the softer the collagen network was (**Supplementary Fig. 5G**).

Organizational structure of collagen network

The spatial organization of the collagen fibres to form into a fibrotic wall is still unknown. Therefore, we assumed six different scenarios (S) of the organizational structure of collagen network: the collagen fibres are deposited as single fibres and not anchoring to the nearest sinusoids in S1; as single fibres and anchoring to the nearest sinusoids in S2; as single fibres and crosslinked to form a network, but not anchoring to the nearest sinusoids in S3; as single fibres and crosslinked to form a network, and anchoring to the nearest sinusoids in S4; as single fibres firstly and gradually crosslinked to form a network, but not anchoring to the nearest sinusoids in S5; as single fibres firstly and gradually crosslinked to from a network, and anchoring to the nearest sinusoids in S6 (**Supplementary Fig. 9A**). One simplified section of the two-lobules system without HSC and Mph in DT (the lesion region of the section was set in the middle of the section, with the width of 4 hepatocytes' diameter) was run for 21 days to test these scenarios. The initial lesion size was set as 45 μm (in y-axis). Six rounds of CCl_4 were injected at day 0, 3, 7, 10, 14, 17, respectively. At the moment of the second injection, namely, day 3, all collagen fibres were generated homogeneously distributed in the lesion. The total length of generated collagen fibres are calculated according to one given collagen density (see section of **Network generation approach** for details of transforming the density into the total length of fibres). Hepatocytes outside of the lesion region proliferated to fill up the lesion and compressed the fibres (the proliferation rate data is from **Hoehme et al. 2010**). For each scenario, we studied three different collagen densities: 0.4 mg/mL, 1.0 mg/mL, and 2.0 mg/mL. The deformation of the collagen network was measured by its gyration radius in y-axis (see section of **Measurement of the height of the collagen network**). For each scenario with each density, three simulation runs were performed to calculate the average and standard deviation.

Our results showed that in S1 the proliferating hepatocytes resulted mainly in a displacement of the fibres, or passed in between the fibres, so that part of the fibres remained between the hepatocytes (scenario 1 in **Supplementary Fig. 9B-D**). In S2 fibres anchored to the sinusoids. They can partially resist hepatocyte movement as they bend upon contact with the hepatocytes (scenario 2 in **Supplementary Fig. 9B-D**, gyration radius curve in **Supplementary Fig. 9E-G**). The difference between S3 and S4 was similar to that between S1 and S2. This can be attributed to the fact that the crosslinked fibres were integrated into one scaffold that was much more difficult to be displaced or compressed than individual fibres, as long as cells cannot push or pass the network. In addition, in S4, fibres were anchored to the sinusoids, so it was even more difficult for hepatocytes to deform them (reflected by the gyration radius curve in **Supplementary Fig. 9E-G**, scenarios 3 & 4 in **Supplementary Fig. 9B-D**). Moreover, as we increased the collagen density from 0.4 mg/mL to 2.0 mg/mL, the fibre network was more resistant to the penetration of proliferating hepatocytes. In the case of the highest collagen density (2.0 mg/mL), the network was barely deformed compared to those with lower densities (**Supplementary Fig. 9D** and gyration radius curve in **Supplementary Fig. 9G**). In S5, fibres were compressed and concentrated in the middle of the lesion region and formed a wall-like structure (scenario 5 in **Supplementary Fig. 9B-D**). This can be attributed to the fact that the fibre network was formed through crosslinks gradually. So compared to the network which was formed immediately through crosslinks in S3, it was easier to be deformed. In addition, since all of the fibres were eventually crosslinked, they were not distributed scatteredly as seen in S1 and 2. Moreover, under each collagen density, the thickness of the fibre network in S5 was among the thinnest (gyration radius curve in **Supplementary Fig. 9E-G**). In S6, the fibre network was more resistant to the penetration of proliferating hepatocytes than that in S5 (scenario 6 in **Supplementary Fig. 9B-D**). This was due to the fact that the fibres were anchored to the nearest sinusoids.

These simulation results suggest that the crosslinks between collagen fibres are important to maintain the elastic property of the collagen network. Otherwise, fibres without crosslinks cannot remain as integrity against the penetration of proliferating hepatocytes (**Supplementary Fig. 9B-D**). However, if the crosslinks are formed too early or if the fibres can anchor to the sinusoids, the network is highly resistant to the compression from hepatocytes. Among all six scenarios of organizational structure of collagens, scenario (5), namely, collagen initiated as single fibres and gradually crosslinked but not anchoring to the closest sinusoids looks to be the optimal one for our simulation of fibrosis process. In addition, the collagen network under low density (0.4 mg/mL) is too sparse to form a thick wall-like structure as observed in experiments (Fig. 1A) while the network under high density (2.0 mg/mL) is too dense for hepatocytes to deform (**Supplementary Fig. 9D**). Therefore, we took the median density 1.0 mg/mL for our next simulation.

Production and degradation of collagen fibres by HSC and Mph. During liver fibrosis, excessive amounts of ECM proteins are secreted by activated HSC (**Ghosh et al. 2013**). Collagen fibres are degraded by macrophages (**Madsen et al. 2013**). We modeled the whole procedure of the migration of HSC and macrophages into the lesion, producing and degrading collagen fibres, respectively.

Signal-gradient based migration of HSC and macrophages. Previous studies have reported that injured hepatocytes can produce DAMP signals to activate macrophages (**Calderwood et al. 2016**, **Martin-Murphy et al. 2010**). Here we assumed that DAMP is produced by necrotic hepatocytes. HSC

and Mph migrate towards the local gradient of DAMP (**Supplementary Fig. 7A**). The concentration of DAMP ϕ_{DAMP} is updated by solving a partial differential equation (PDE):

$$\frac{\partial \phi_{DAMP}}{\partial t} = \nabla(D_{DAMP}\nabla\phi_{DAMP}) + s_{DAMP}(\sum_j \delta(x - x_j)) - \gamma_{DAMP}\phi_{DAMP}, \quad (16)$$

where D_{DAMP}, s_{DAMP}, γ_{DAMP} are the diffusion coefficient, production rate, decay rate of DAMP, respectively; x_j denotes the position of necrotic hepatocyte j, which produces DAMP. The center of mass of j is set as the origin of the source. The simulation domain Ω is set as a box large enough to contain the entire lobule. For one macrophage or HSC i, if its local concentration of DAMP is higher than a threshold, a migration force $\vec{F}_{mig,i} = f_{mig,i}\frac{\nabla\phi_{DAMP,i}}{\|\nabla\phi_{DAMP,i}\|}, f_{mig,i} \sim N(F_{mig,i,mean}, F_{mig,i,sd})$ is then applied on i, where $F_{mig,i,mean}$ and $F_{mig,i,sd}$ are the mean and standard deviation of migration force magnitude calibrated from the mean and standard deviation of migration speed of i (**Tangkijvanich et al. 2001**; **Grabher et al. 2007**).

Production of collagen fibres. Previous studies have reported that HSC proliferates and becomes activated. Activated HSC is the major source of collagens and other matrix proteins (**Iredale et al. 1998**). It is also documented that the recovery from liver fibrosis is accompanied by apoptosis of activated HSC (**Kisseleva et al. 2012**). Here we assumed that after each dose of CCl_4 injection, HSC in the lesion proliferated. After cell division, the daughter HSC was activated while the mother HSC was killed. This is to ensure that the total number of HSC remains the same. The activated HSC can produce collagen fibres. We observed that after the second dose of CCl_4, collagen fibres are gradually accumulated within one day after the injection. Denote the coordinates of the head spheres of activated HSC as $V_{aHSC} \equiv \{x_i\}$. For a given collagen mass density ρ_c, the total length of deposited collagen fibre is L_{tot}. The fibres are produced evenly within one day after the injection of CCl_4. For one deposited fibre j, the initial position $x_{j,0}$, is sampled randomly from V_{aHSC} by HSC i, which satisfies $\left|\left|x_{j,0} - x_i\right|\right| < L_{i,HSCB}$, where $L_{i,HSCB}$ is the length of the HSC branch of i. The choice of initial tangent direction and direction of extending segment of j is the same as that in the section of **Network generation approach**.

Degradation of collagen fibres. We observed that F4/80 expressed macrophages only start to appear 12 hours after the injection of CCl_4. We assumed that macrophages in the lesion displayed F4/80 negative phenotype within 12 hours after the injection of CCl_4 and switched to F4/80 positive phenotype 12 hours after the injection. To mimic the digestion process, for each F4/80 positive phenotype macrophage i, if its distance with one collagen fibre segment j satisfies $d_{ij} < r_i + r_j$, where r_i is the radius of i and r_j is the radius of j, then j is removed from the system. Since previous study has reported that the engulfment time of macrophage is about 3 hours (**Haecker et al. 2002**), we assume that one F4/80 positive macrophage is only able to digest fibres 3 hours after it engulfs one fibre.

Digestion of dead hepatocytes by macrophages. As shown in **Supplementary Fig. 6B**, the AST level (partially correlated with the number of necrotic cells) after the second dose of CCl_4 is only 1/10 of that after the first dose of CCl_4. As shown in **Fig. 2A** (HE & IgG staining), after the first dose of CCl_4, there are no more than 10 layers of hepatocytes dying due to intoxication. Therefore, we assumed that after the second dose of CCl_4, there is only one layer of necrotic hepatocytes in the middle of the lesion. The F4/80-positive macrophage can digest the necrotic hepatocytes. To mimic the digestion process, for each F4/80-positive macrophage i, if its distance with one necrotic hepatocyte j satisfies $d_{ij} < r_i + r_j$, where r_i is the radius of i and r_j is the radius of j, then j is removed from the system. Since the previous study has reported that the engulfment time of macrophage is about 3 hours (**Haecker et al. 2002**), we assume that one F4/80 positive macrophage is only able to digest the necrotic hepatocyte 3 hours after it engulfs one necrotic hepatocyte.

Supplementary Table 2. DT parameters.

Description	Value	Reference
Hepatocyte radius	~10.7 μm	Estimated from data
Sinusoid radius	~2.1 μm	Hoehme et al., 2010
HSC radius	~2 μm	Wake, 2006
HSC branch length	~12 μm	Wake, 2006

Mph radius	~6 µm	Shi et al., 2011
Collagen fibre radius	~0.1 µm	Wenger et al., 2007
Collagen fibre segment length	~3 µm	Stein et al., 2008
Young's modulus of hepatocyte	~400 Pa	Hoehme et al., 2010
Young's modulus of sinusoid	~600 Pa	Hoehme et al., 2010
Young's modulus of HSC	~700 Pa	Estimated from fibroblast, Yang et al., 2012
Young's modulus of macrophage	~1400 Pa	Estimated from immune macrophage, Bufi et al., 2015
Young's modulus of collagen fibre	~50 MPa	Manssor et al., 2016
Poisson ratio of all components	0.4	Hoehme et al., 2010
Cell cycle time of hepatocyte	24 hours	Hoehme et al., 2010
Cell cycle time of HSC	24 hours	Estimated
Medium friction for hepatocyte, sinusoid and macrophage	10^8 Ns/m^3	Estimated
Medium friction for HSC	10^{10} Ns/m^3	Estimated
Medium friction for collagen fibre	10^{11} Ns/m^3	Estimated
Friction between all components	10^8 Ns/m^3	Estimated
HSC density in the liver	~1/70 µm of the sinsoid	Wake, 2006
Mph density in the liver	~2×10^4/mm^3	Bouwens et al., 1986
Collagen density	~1 mg/ML	Stein et al., 2008
Mean of migration speed of HSC	~2.1 µm/hour	Tangkijvanich et al., 2001
SD of migration speed of HSC	~0.1 µm/hour	Tangkijvanich et al., 2001
Mean of migration speed of Mph	~5 µm/min	Grabher et al., 2007
SD of migration speed of Mph	~1.8 µm/min	Grabher et al., 2007
Diffusion rate of DAMPs, estimated from its molecular weight, 28 kDa	~2.5×10^{-11} m^2/s	Davies et al., 2018

Decay rate of DAMPs, estimated from its half-life, ~1000 seconds	~5.7×10^{-4} /s	Zandarashvili et al., 2013
Fraction of HSC switching to inverted phenotype	0.5	Kisseleva et al., 2012
Fraction of apoptosis HSC after each injection of CCl_4	0.5	Kisseleva et al., 2012
Time of macrophage switching to $Ly6C^{low}$ phenotype after each injection of CCl_4	12 hours	Estimated from data
Engulfment and elimination duration of Mph	~3 hours	Estimated from Haecker et al., 2002
The width of the lesion size	~80 μm	Estimated from data

Supplementary Figures

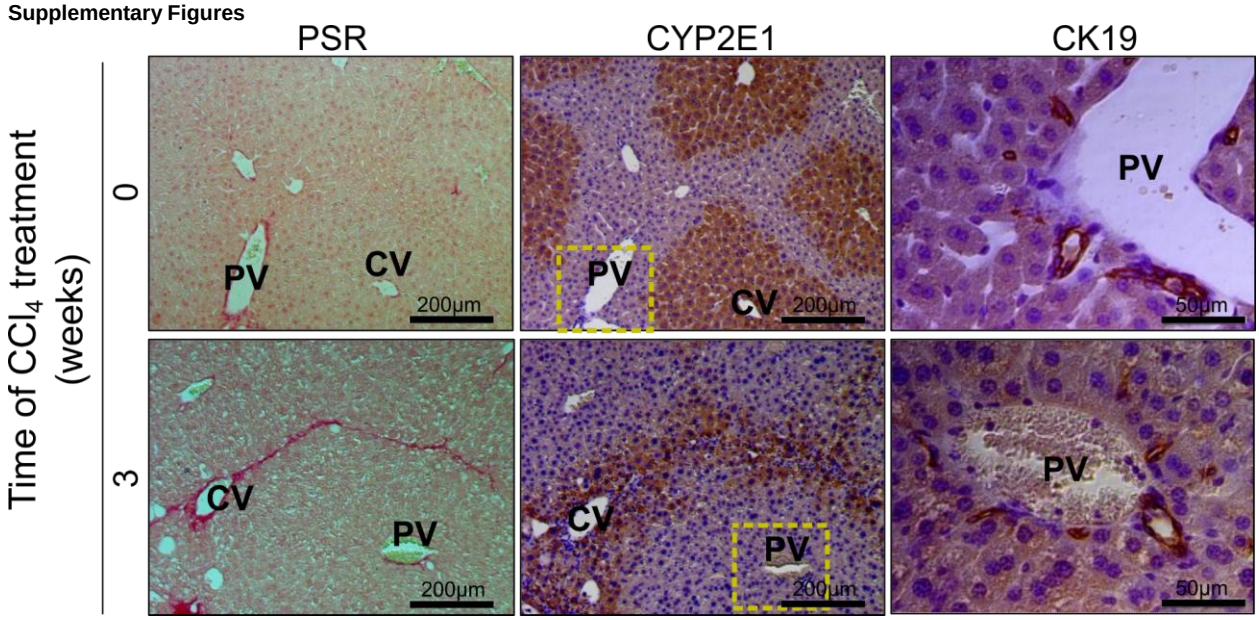

Supplementary Figure 1. CYP2E1 expressing hepatocytes guide ECM deposition upon repetitive CCl_4 injections. Serial sections from control and fibrotic mouse liver (3 weeks of CCl_4) were stained with PSR (ECM deposition; red), CYP2E1 (CCl4 metabolizing enzyme; brown) and CK19 (bile duct epithelial cell marker in periportal compartments). Scale bars are 200µm (PSR and CYP2E1 images) and 50µm (CK19 images).

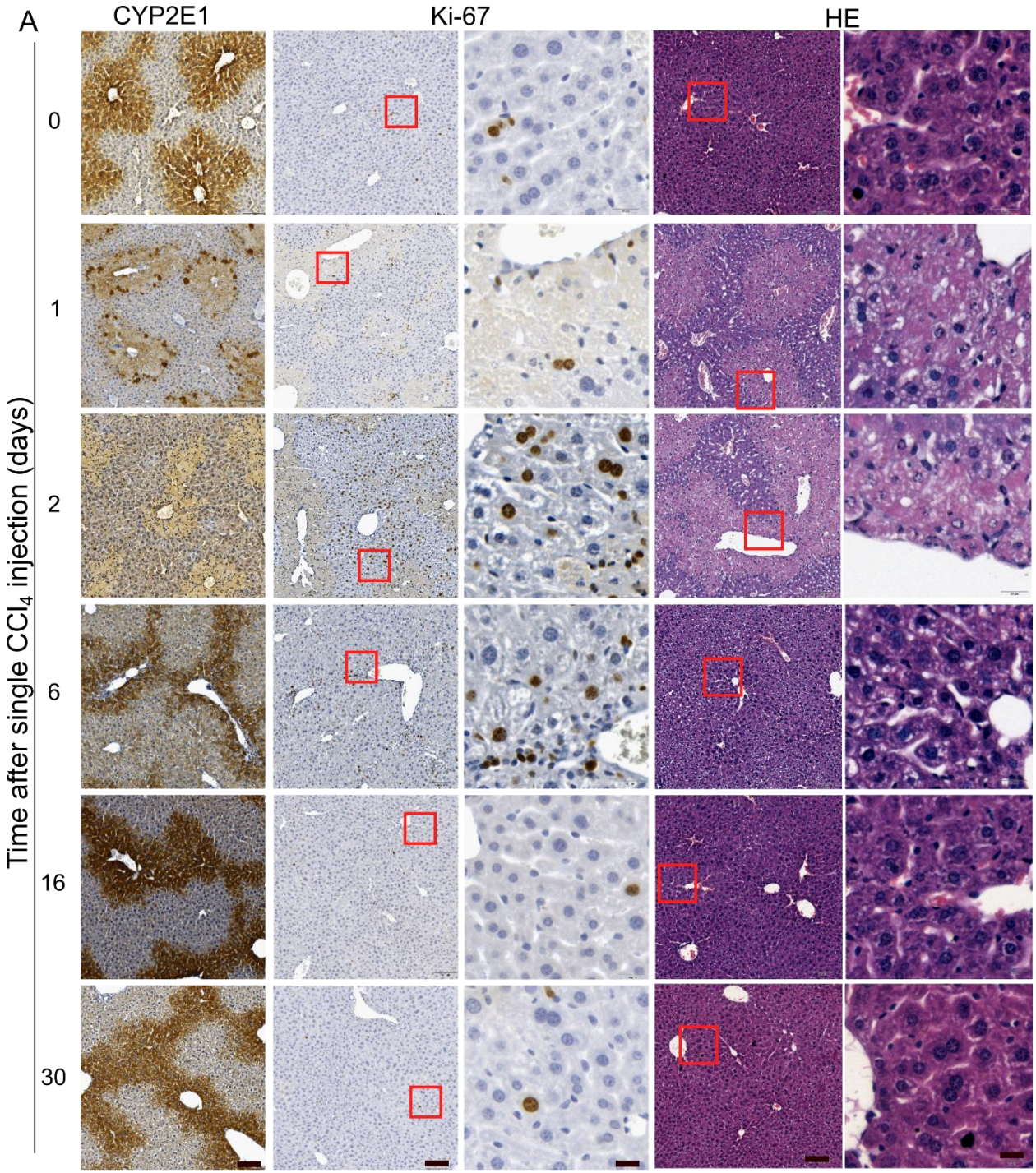
A
CYP2E1
Ki-67
HE
Time after single CCl4 injection (days)
0
1
2
6
16
30

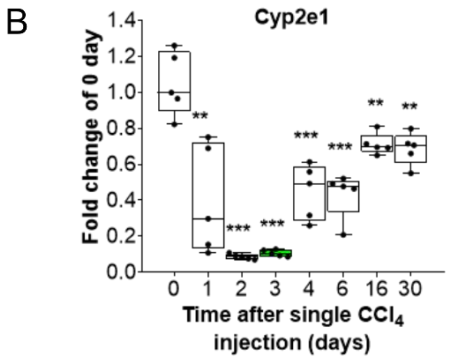
B
Cyp2e1
Fold change of 0 day
1.4
1.2
1.0
0.8
0.6
0.4
0.2
0.0
0 1 2 3 4 6 16 30
Time after single CCl4 injection (days)

Supplementary Figure 2. Regeneration upon acute liver injury in mice from one CCl_4 injection. (A) Representative time-resolved images of CYP2E1, Ki-67 and HE stained livers upon one dose of CCl_4. Scale bars are 100µm and 20µm for overviews and closeups, respectively. (B) mRNA level of Cyp2e1, determined at different time points after administration of CCl_4 as indicated. Data are shown as the means ± SD of 5 mice per group. The values at day 0 represent the controls. ** P <0.01, *** P <0.001.

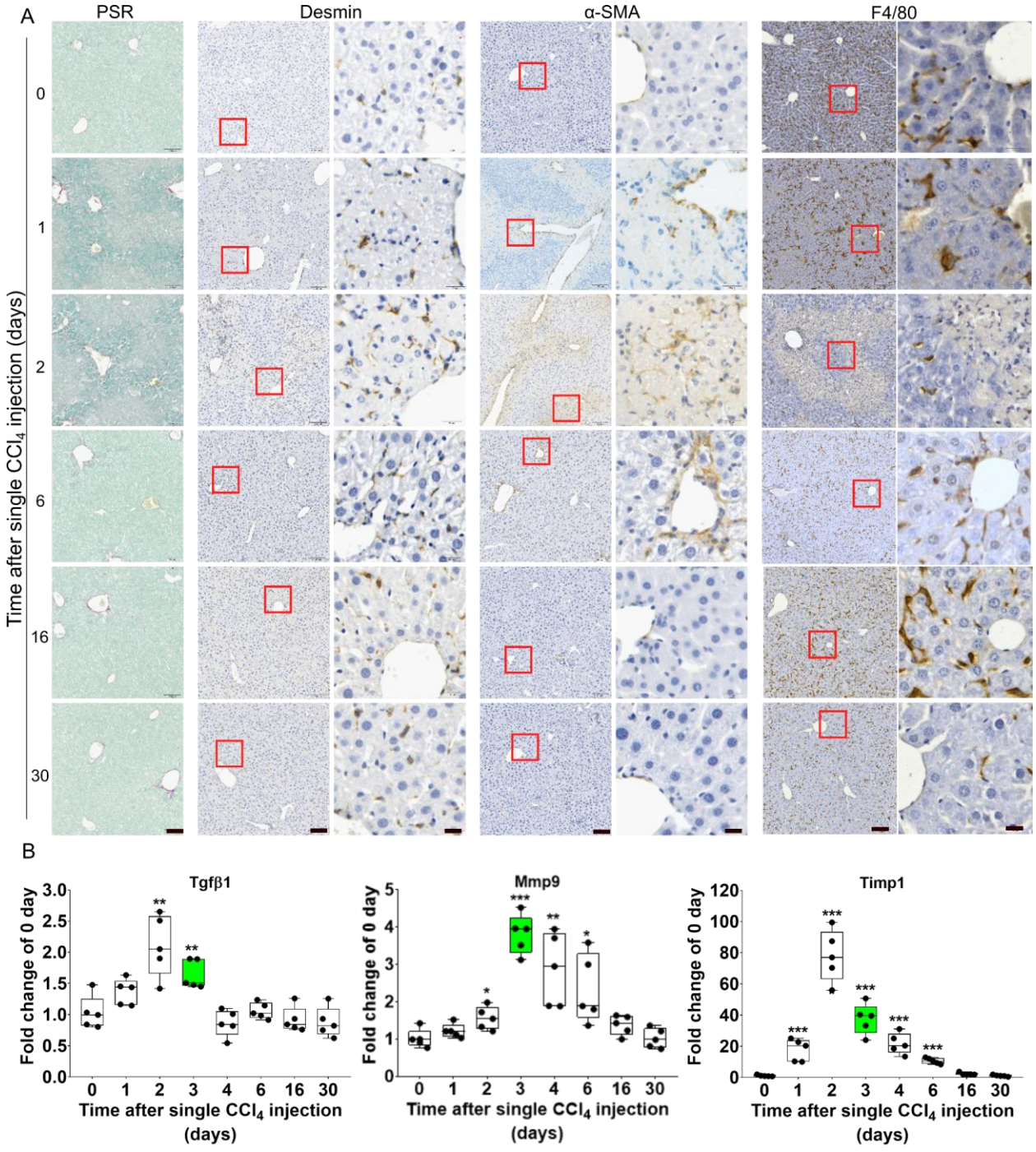

Supplementary Figure 3. ECM, HSC and macrophages during liver regeneration upon one CCl_4 injection. (A) Time-resolved histopathological data after a single CCl_4 injection, showing PSR (ECM), desmin (quiescent and activated HSC), α-SMA (activated HSC), F4/80 (resident macrophages). Desmin, α-SMA and F4/80 are each displayed at overview-magnification (left, scale bar 100µm) and high magnification for closeup (right, scale bar 20µm). (B) Time resolved RT-PCR data for Tgfβ1, Mmp9 and Timp1. Data are shown as the means ± SD of 5 mice per group. * P <0.05, ** P <0.01, *** P <0.001.

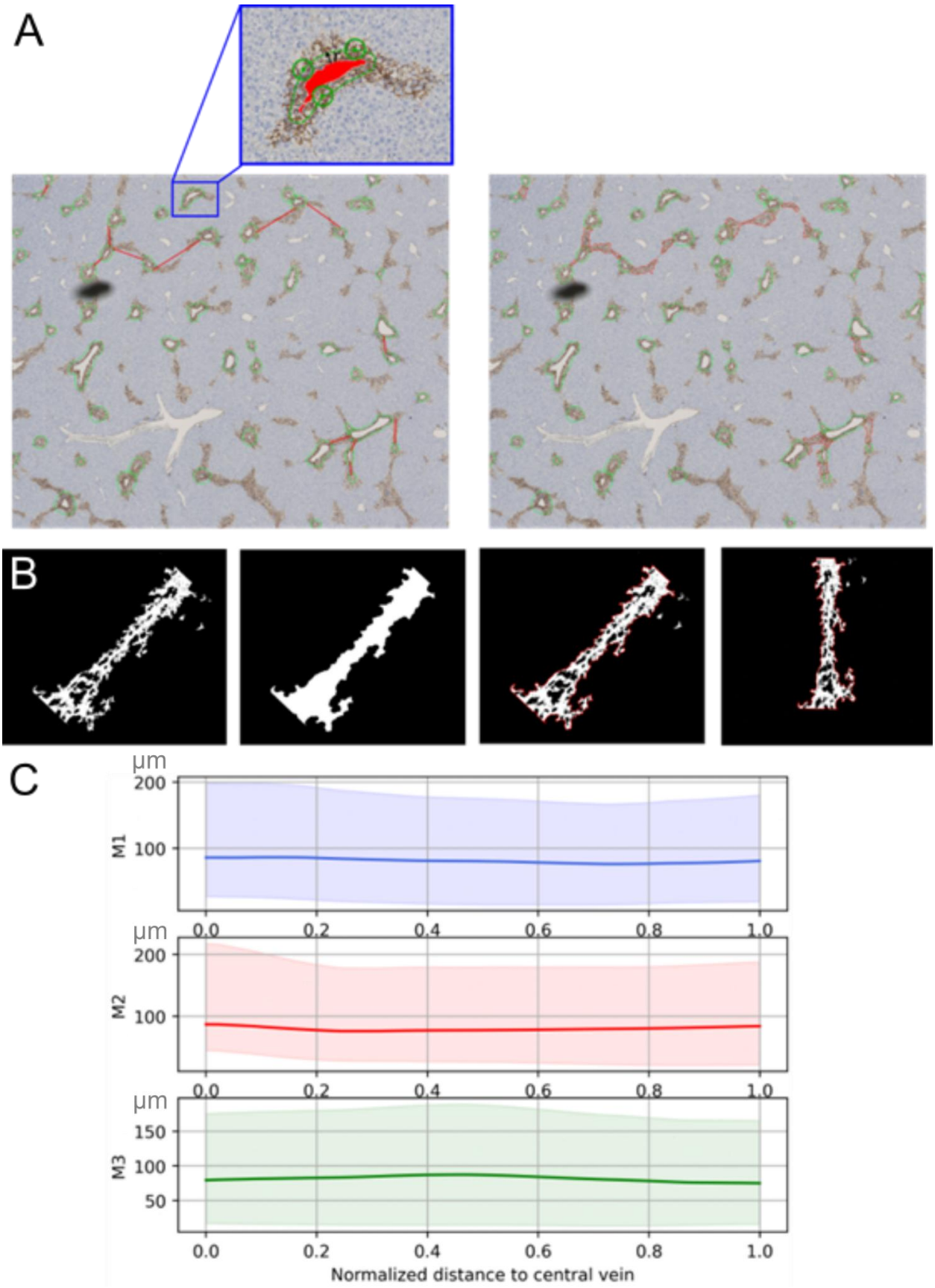
A
B
C
µm
200
100
M1
0.0
0.2
0.4
0.6
0.8
1.0
µm
200
100
M2
0.0
0.2
0.4
0.6
0.8
1.0
µm
150
100
50
M3
0.0
0.2
0.4
0.6
0.8
1.0
Normalized distance to central vein

Supplementary Figure 4. **Computation of the distribution of the spanning width of α-SMA positive cells.** (A) Example of a region of interest showing the activated HSCs in brown; brown regions with void representing CVs are marked by green circles. In the left subfigure, the red lines are drawn manually to identify neighboring CVs connected by areas occupied by activated HSCs; in the right subfigure the red curved lines demarcate the borders of these areas ("stripes"). (B) The different steps to obtain the envelope (border) of an aHSC positive area (stripe) connecting two neighboring CVs. Each stripe is finally oriented vertically before computing its spanning width along the axis starting at one CV and ending at the neighboring CV. (C) The resulting values for the width of the stripe along the CV-CV connection is then normalized by division of the length of the CV-CV connection to permit accumulation of the data for CV-CV connections of different lengths (shown are accumulated data, each from multiple CV-CV connections from different mice M1, M2, and M3). Interestingly, the width of the stripes do not vary along the CV-CV connection.

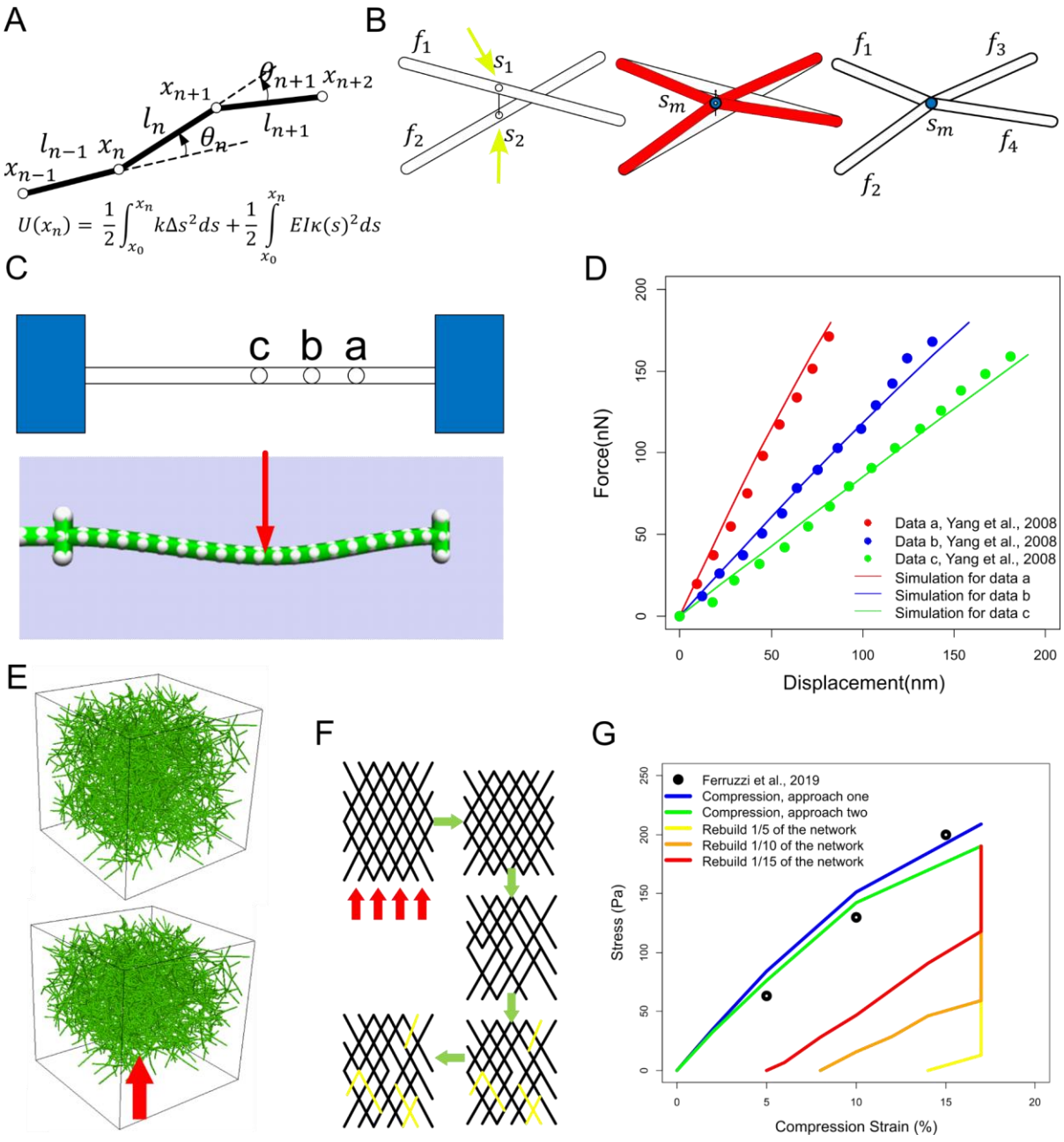

Supplementary Figure 5. **Construction and validation of the collagen (ECM) model**. (A) Elastic and bending energy of the collagen fibre network. (B) Addition of crosslink nodes: If the distance between two fibre segments f_1 and f_2 (between two

perpendicular nodes s_1 and s_2 on f_1 and f_2, respectively, indicated by yellow arrows) is smaller than a predefined threshold, one crosslink node s_m (blue) is added, where f_1 and f_2 would crosslink (red). After crosslinking, the segments are re-enumerated: f_1 and f_2 are divided generating two additional segments (f_3 and f_4), which are all attached at s_m (blue). (C) Calibration of mechanical parameters for the bundles mimicking the bending test by Yang, et al, 2008. 'a', 'b', and 'c' indicate the corresponding positions where the force is applied on the fibre. The simulated fibre (length of 3 µm) bends upon the exerted force (red arrow). (D) Simulation result and experimental data from Yang et al., 2008. (E) The modeled compression of the collagen network. The size of the network is 42.8×42.8×42.8μm^3. The network is compressed by fixing the collagen nodes on the top layer and moving the bottom layer of collagen nodes upwards. (F) Rebuild the network for plasticity test: After the 3D network of cross-linked fibres (from D,E) is compressed, some fibres are randomly removed from and subsequently randomly added back to the network; subsequently, the compressed network is relaxed. This algorithm mimics a visco-elastic network with a plastic response. (G) Strain-stress curve of simulation and experimental data from Ferruzzi et al., 2019. Different fractions of total fibres rebuilt (removed first and then added back) in the network are tested.

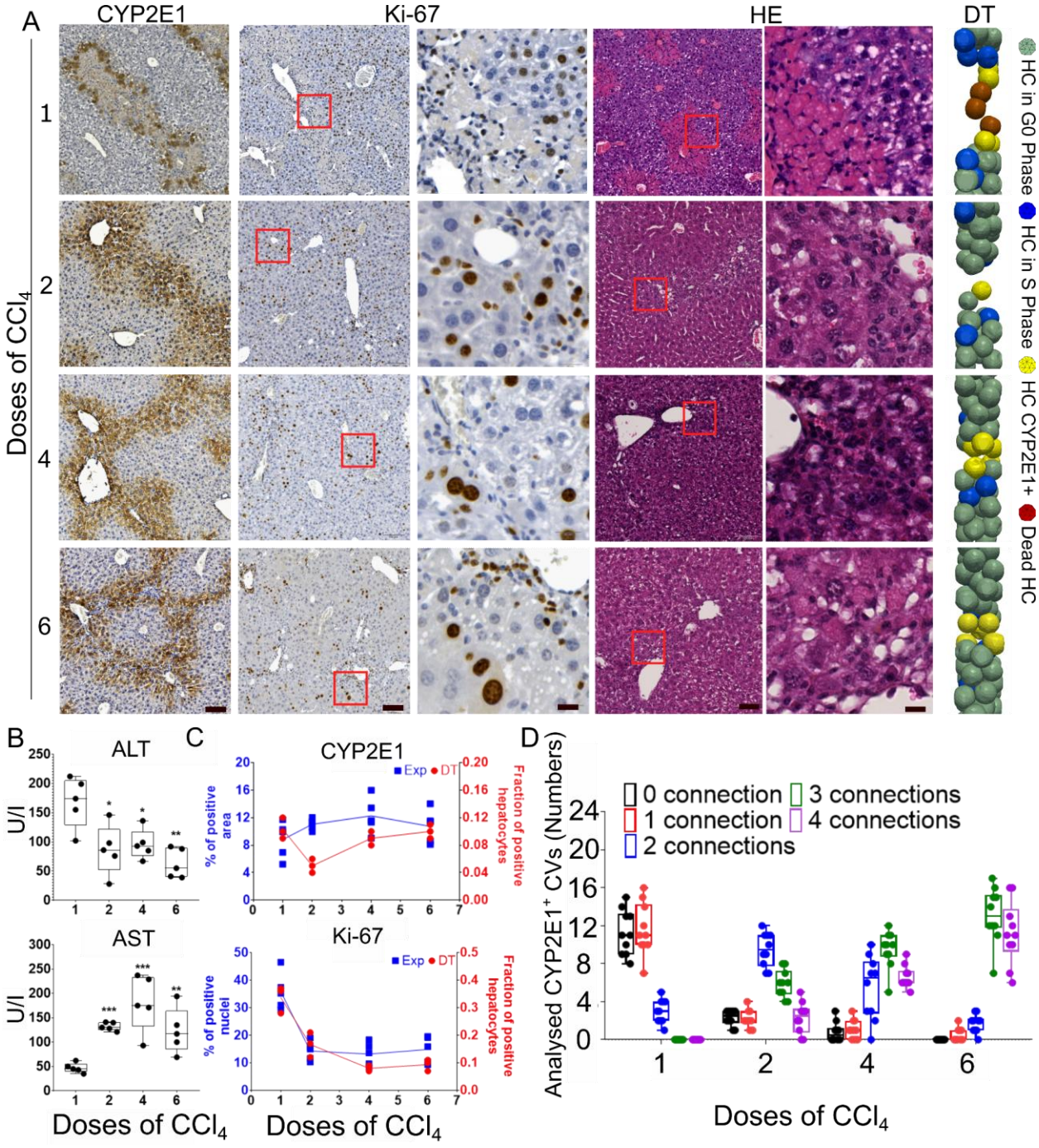

Supplementary Figure 6. Chronic liver injury in mice from 6 injections of CCl_4. (A) Representative images of CYP2E1, Ki-67 and HE stained livers plus snapshots of the DT for repeated doses of CCl_4 (scale bars are 100µm for overview and 20µm for closeup images). The corresponding days are day 3 (3 days after dose 1), 7 (4 days after dose 2), 14 (4 days after dose 4), 21 (4 days after dose 6). (B) Blood levels of liver transaminases (AST and ALT), upon repetitive CCl_4 injections. (C) (Top) Quantification of the experimentally determined CYP2E1 positive area and fraction of CYP2E1 positive cells in the DT. (Bottom) Quantification of Ki-67 positive nuclei and fraction of S-phase hepatocytes in the DT. (D) Quantification of CVs connected by CYP2E1 positive hepatocytes. Experimental data are shown as the means ± SD of 5 mice per group. * P <0.05, ** P <0.01, *** P <0.001. DT simulation data are shown as the means ± SD of 3 independent simulation runs.

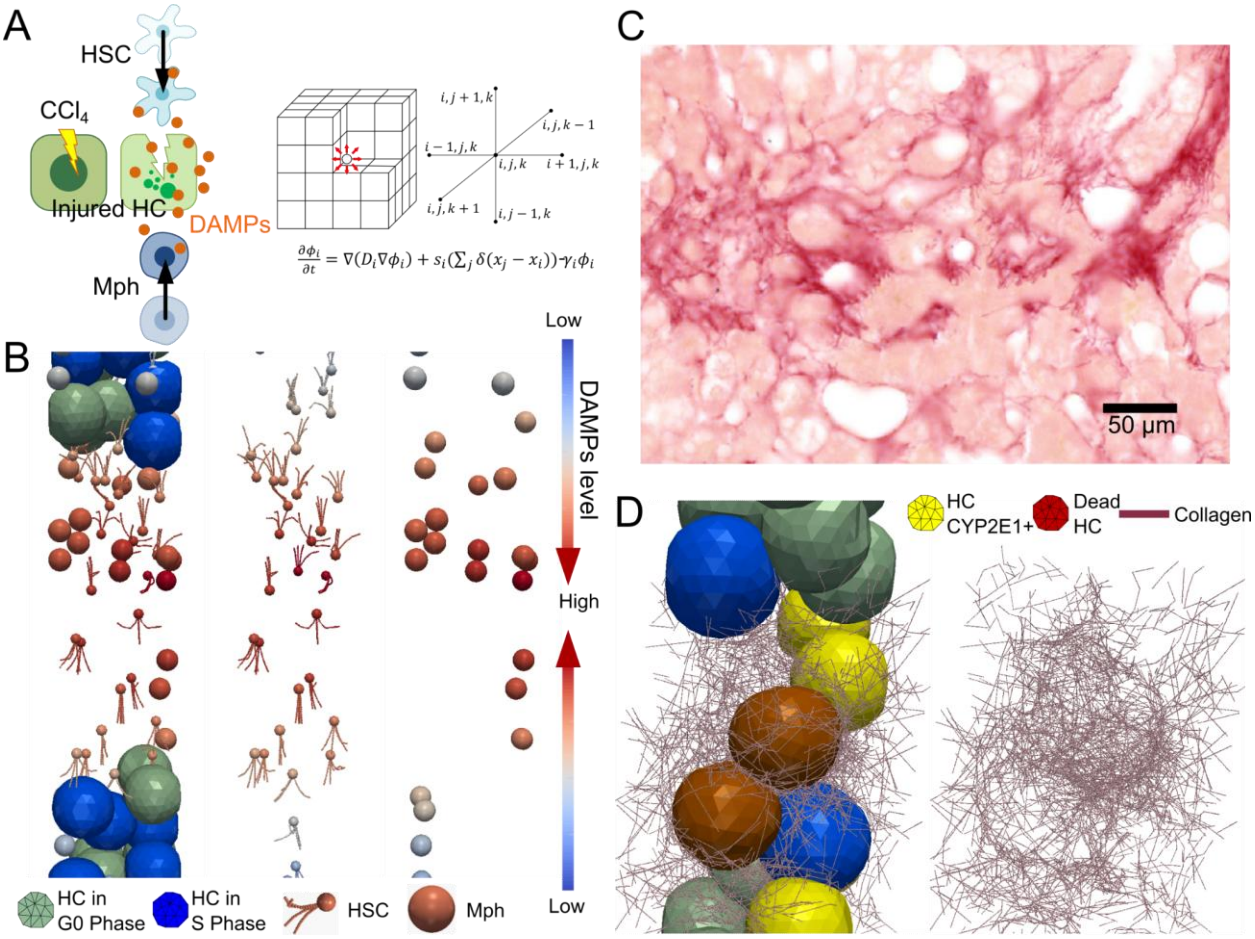

Supplementary Figure 7. **Migration of HSC and Mph to mediate liver fibrosis formation.** (A) Scheme of DAMPs gradient in the model (DT). Injured HC produce DAMPs. DAMPs can activate HSCs and macrophage (Mph) to migrate towards the largest DAMP gradient. The spatio-temporal DAMP concentration is calculated by solving a differential equation that takes into account synthesis, diffusion, and decay of DAMPs. The differential equations were solved in a discretized cubic system. (B) Snapshots representative for migrating HSCs and Mphs from low (blue) to high (red) DAMP concentrations (**Supplementary Movie 3**). (C) Chicken wire pattern of liver fibrosis (collagen fibres wrap liver cells), as observed in NASH mouse model. Scale bars are 50μm. (D) Chicken wire pattern, as captured by the DT. Left: collagen fibres wrapping HC; Right: the same structure in left by excluding the HC.

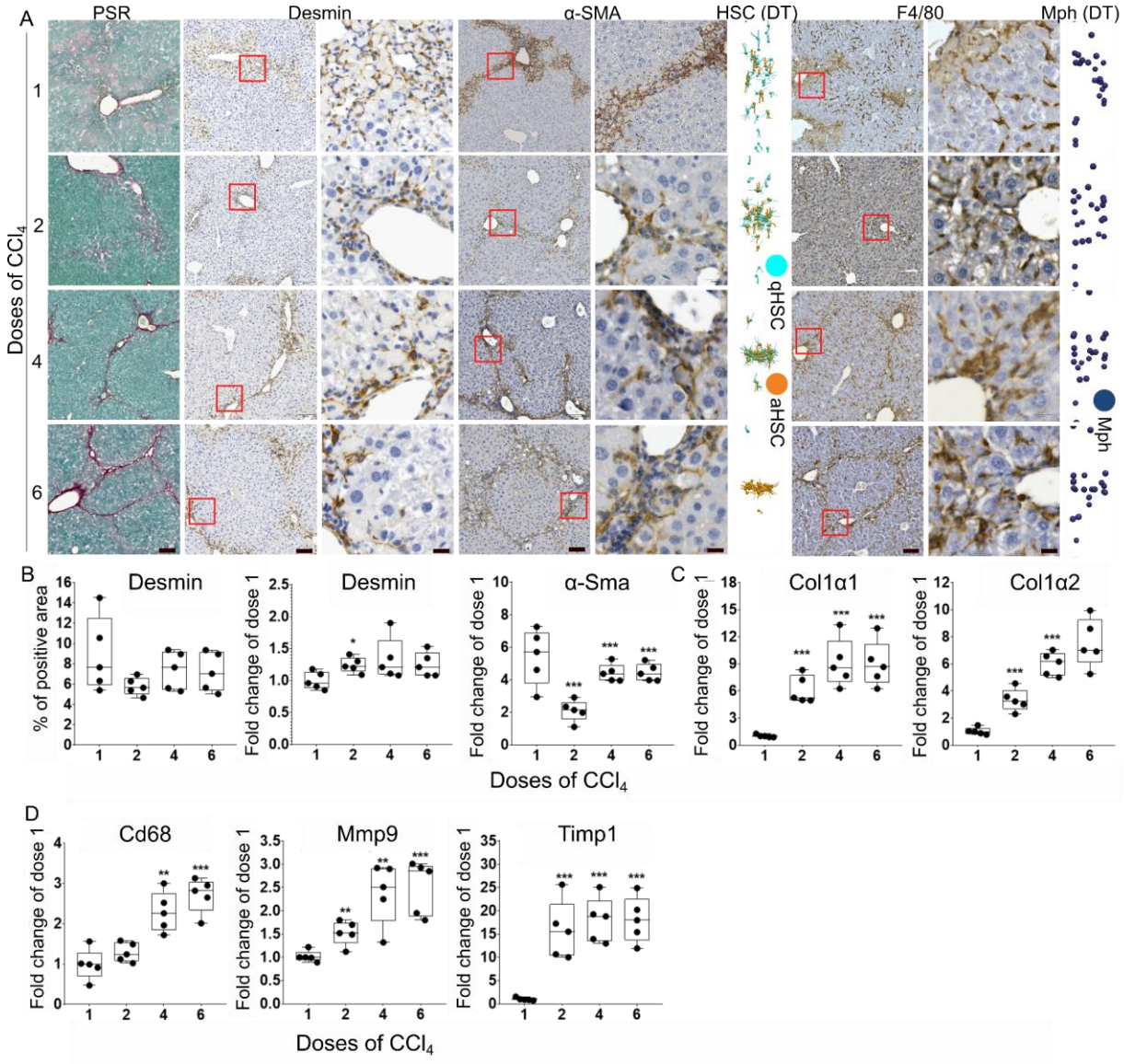

Supplementary Figure 8. HSC, Mph and matrisome analysis in the dynamics of CCl_4 mediated chronic liver disease. (A) Representative images of PSR, desmin, α-SMA, and F4/80 stained livers and snapshots of HSC and Mph in the DT simulation. (B-D) Protein/mRNA levels of desmin, α-SMA, Collagen1α1, Collagen1α2, Cd68, Mmp9, and Timp1 determined by IHC or RT-PCR, as indicated. Scale bars are 100μm for overview and 20μm for closeup images. Experimental data are shown as the means ± SD of 5 mice per group. * P <0.05, ** P <0.01, *** P <0.001. DT simulation data are shown as the means ± SD of 3 independent simulation runs.

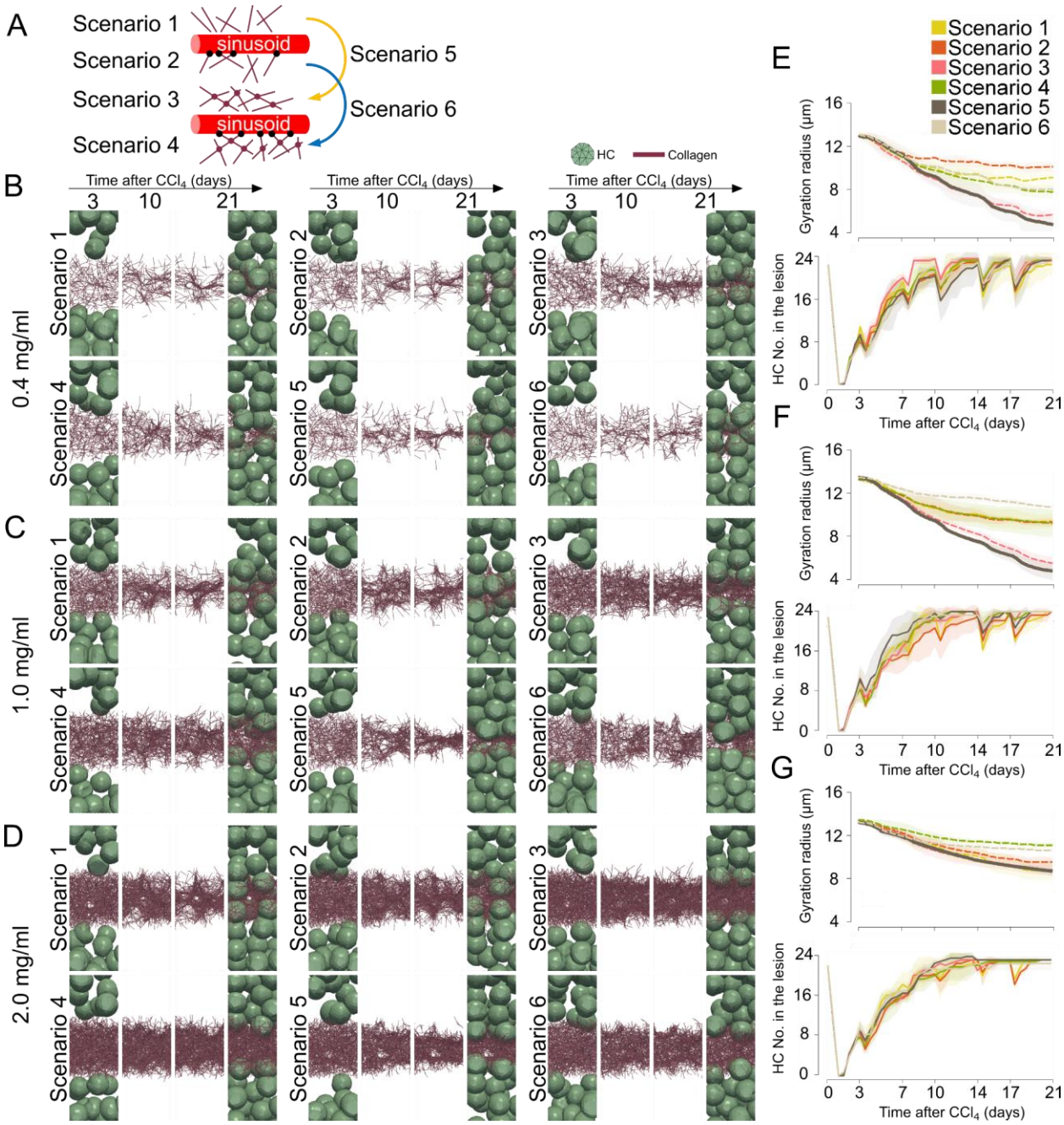

Supplementary Figure 9. **Organizational structure of the collagen network**. (A) There are six scenarios (S) for the structure of collagen deposition. Collagen fibres are deposited as single fibres in S1, single fibres anchored to the nearest sinusoids in S2, crosslinked single fibres in S3, crosslinked single fibres anchored to the nearest sinusoids in S4. In S5, collagen fibres are firstly deposited as single fibres and then gradually crosslinked while in S6, collagen fibres are firstly deposited as single fibres anchored to the nearest sinusoids and then gradually crosslinked. (B-D) Snapshots of collagen fibre organization as resulting from the different simulation scenarios with the DT based on assuming collagen densities of 0.4 mg/mL, 1.0 mg/mL and 2.0 mg/mL, respectively. (E-G) Gyration radius of the fibres and number of hepatocytes in the lesion in the different scenarios. Scenario 5 in the graph depicting the gyration radius is highlighted in a solid line, while the other scenarios are presented in dashed lines. The error bars represent the standard deviation of 3 simulation runs.

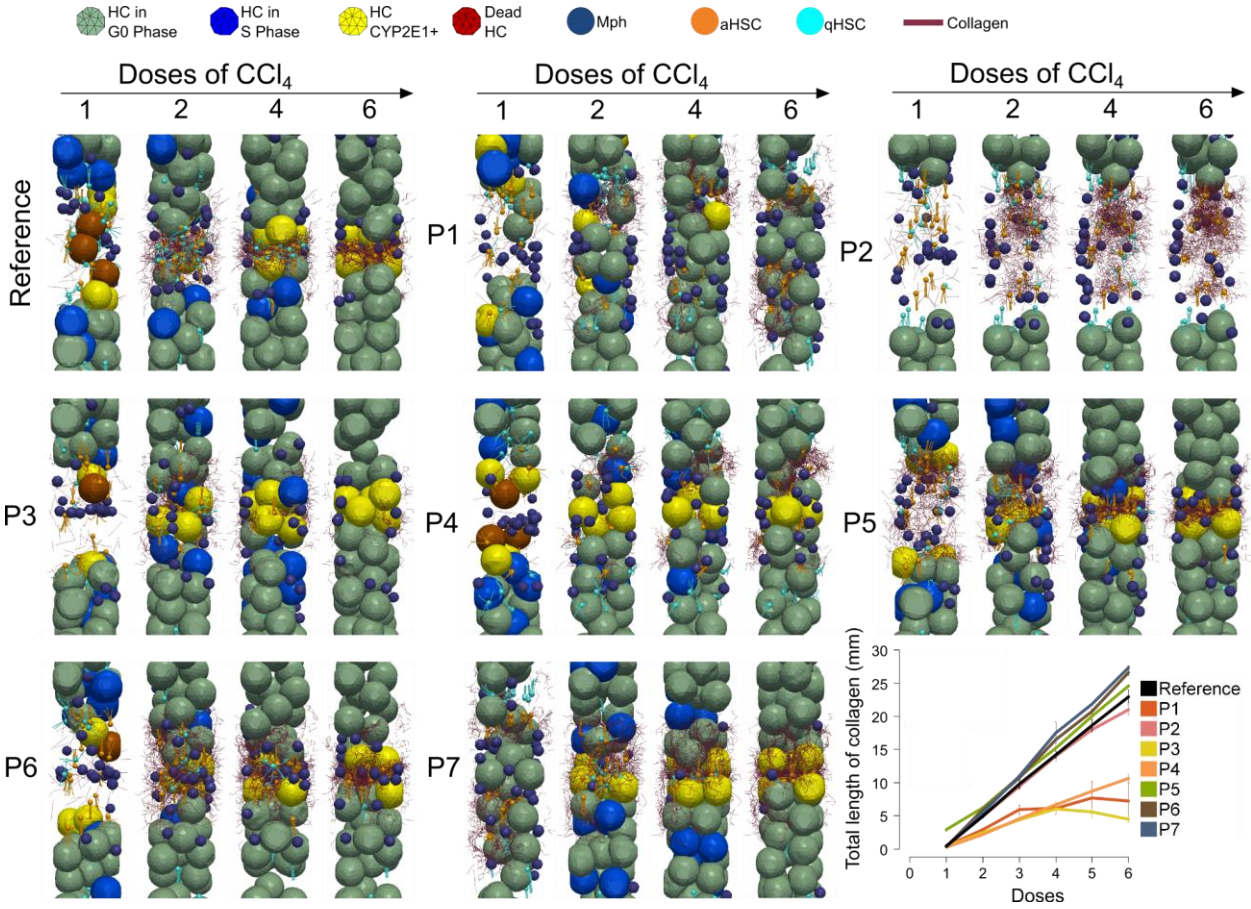

Supplementary Figure 10. **Snapshots of DT simulation result from the different perturbation runs**. Seven perturbation scenarios were tested. P1, random distribution of CYP2E1+ hepatocytes; P2, lack of hepatocyte proliferation; P3, 70% of activated HSC undergo cell death; P4, HSC are not able to migrate; P5, HSC display an inverted phenotype after CCl4 injections; P6, macrophages become Ly6C^{low}, 5 days after CCl_4 injections, and P7, macrophages cannot migrate. Typical time-lapse DT simulations are shown as **Supplementary Movies 4-10**. The plot of total length of collagen after doses of CCl_4 under each perturbation is also shown.

Supplementary Movies

Supplementary Movie 1. 3D reconstruction of one hepatocyte (yellow), nucleus (blue) and wrapped by sinusoids (red). This cell reconstruction is generated from confocal images obtained from healthy mouse liver (**Hammad et al. 2014**).
https://drive.google.com/file/d/1hjHQyXlTWBnoNKrUQ0g2HYwYx3GALgaZ/view?usp=sharing

Supplementary Movie 2. Time-Lapse video of a typical model simulation of the formation of fibrotic pattern in the reference model (Light green: healthy hepatocyte; Yellow: CYP2E1+ hepatocyte; Brown: dead hepatocyte; Blue: dividing hepatocyte; Dark Blue: Mph; Cyan: qHSC; Orange: aHSC; Dark purple: collagen fibre).
https://drive.google.com/file/d/1Ssj74yrO_4PqQyhHF_uVpF4P2s26-a0J/view?usp=sharing

Supplementary Movie 3. Time-Lapse video of a typical model simulation showing migration of HSC and Mph towards the gradient of DAMPs. Mph is represented as a sphere and HSC is represented as one sphere attached with several chains.
https://drive.google.com/file/d/1CvK58Vb06exL-Ou8UZpaYv_QwVp1iip_/view?usp=sharing

Supplementary Movie 4. Time-Lapse video of a typical model simulation of the perturbation 1 (randomly distributed CYP2E1+ cells) upon the reference model (Light green: healthy hepatocyte; Yellow: CYP2E1+ hepatocyte; Brown: dead hepatocyte; Blue: dividing hepatocyte; Dark Blue: Mph; Cyan: qHSC; Orange: aHSC; Dark purple: collagen fibre).
https://drive.google.com/file/d/17wadrsvQLZKPYw4AqdoSeCVrpqxfnZzs/view?usp=sharing

Supplementary Movie 5. Time-Lapse video of a typical model simulation of the perturbation 2 (no hepatocyte proliferation) upon the reference model (Light green: healthy hepatocyte; Yellow: CYP2E1+ hepatocyte; Brown: dead hepatocyte; Blue: dividing hepatocyte; Dark Blue: Mph; Cyan: qHSC; Orange: aHSC; Dark purple: collagen fibre).
https://drive.google.com/file/d/1oNozUpRhZTA6O4113bqAe4f50iJNe2te/view?usp=sharing

Supplementary Movie 6. Time-Lapse video of a typical model simulation of the perturbation 3 (70% of the activated HSC were killed) upon the reference model (Light green: healthy hepatocyte; Yellow: CYP2E1+ hepatocyte; Brown: dead hepatocyte; Blue: dividing hepatocyte; Dark Blue: Mph; Cyan: qHSC; Orange: aHSC; Dark purple: collagen fibre).
https://drive.google.com/file/d/17wadrsvQLZKPYw4AqdoSeCVrpqxfnZzs/view?usp=sharing

Supplementary Movie 7. Time-Lapse video of a typical model simulation of the perturbation 4 (no HSC migration) upon the reference model ((Light green: healthy hepatocyte; Yellow: CYP2E1+ hepatocyte; Brown: dead hepatocyte; Blue: dividing hepatocyte; Dark Blue: Mph; Cyan: qHSC; Orange: aHSC; Dark purple: collagen fibre).
https://drive.google.com/file/d/1JFw789Bq-4cXRhUFBuOPwXMF8jkKQCdW/view?usp=sharing

Supplementary Movie 8. Time-Lapse video of a typical model simulation of the perturbation 5 (HSC is initiated as inverted phenotype) upon the reference model (Light green: healthy hepatocyte; Yellow: CYP2E1+ hepatocyte; Brown: dead hepatocyte; Blue: dividing hepatocyte; Dark Blue: Mph; Cyan: qHSC; Orange: aHSC; Dark purple: collagen fibre).
https://drive.google.com/file/d/1uzG9oAjKSvpAG85bpu6yiYzAK8AGux86/view?usp=sharing

Supplementary Movie 9. Time-Lapse video of a typical model simulation of the perturbation case 6 (macrophage becomes $Ly6C^{low}$ after 5 days) upon the reference model (Light green: healthy hepatocyte; Yellow: CYP2E1+ hepatocyte; Brown: dead hepatocyte; Blue: dividing hepatocyte; Dark Blue: Mph; Cyan: qHSC; Orange: aHSC; Dark purple: collagen fibre).
https://drive.google.com/file/d/1eWrDYC77_0bwoRXEnItWxEReAjcKe2aZ/view?usp=sharing

Supplementary Movie 10. Time-Lapse video of a typical model simulation of the perturbation 7 (no macrophage migration) upon the reference model (Light green: healthy hepatocyte; Yellow: CYP2E1+ hepatocyte; Brown: dead hepatocyte; Blue: dividing hepatocyte; Dark Blue: Mph; Cyan: qHSC; Orange: aHSC; Dark purple: collagen fibre).
https://drive.google.com/file/d/1amvPhBF9S1e4MbvOv5a2_NHYot-XFHjz/view?usp=sharing

References

Adhyapok, P., Fu, X., Sluka, J.P., Clendenon, S.G., Sluka, V.D., Wang, Z., Dunn, K., Klaunig, J.E., Glazier, J.A. A computational model of liver tissue damage and repair. PLoS ONE 15(12): e0243451 (2020).

Ban, E., Franklin, M., Nam, S., Smith, L.R., Wang, H., Wells, R.G., Chaudhuri, O., Liphardt, J.T., Shenoy, V.B. Mechanisms of plastic deformation in collagen networks induced by cellular forces. Biophys. J. 114(2): 450--461 (2018).

Bouwens, L., Knook, D.L., Wisse, E. Local proliferation and extrahepatic recruitment of liver macrophages (Kupffer cells) in partial-body irradiated rats. Journal of Leukocyte Biology 39: 687—697 (1986).

Bufi, N., Saitakis, M., Dogniaux, S., Buschinger, O., Bohineust, A., Richert, A., Maurin, M., Hivroz, C., Asnacios, A. Human primary immune cells exhibit distinct mechanical properties that are modified by inflammation. Biophysical Journal 108(9): 2181—2190 (2015).

Calderwood, S.K., Gong, J., Murshid, A. Extracellular HSPs: the complicated roles of extracellular HSPs in immunity. Frontiers in Immunology 7: 159 (2016).

Caliari, S.R., Perepelyuk, M., Cosgrove, B.D., Tsai, S.J., Lee, G.Y., Mauck, R.L., Wells, R.G., Burdick, J.A. Stiffening hydrogels for investigating the dynamics of hepatic stellate cell mechanotransduction during myofibroblast activation. Sci. Rep. 6: 21387 (2016).
Cox, R.G. The motion of long slender bodies in a viscous fluid Part 1. General theory. Journal of Fluid Mechanics 44: 791--810 (1970).
Davies, J.E., Apta, B.H.R., Harper, M.T. Cross-reactivity of anti-HMGB1 antibodies for HMGB2. Journal of Immunological Methods 456: 72—76 (2018).
Dichamp, J., Celliere, G., Ghallab, A., Hassan, R., Boissier, N., Hofmann, U., Reinders, J., Sezgin, S., Zuehlke, S., Hengstler, J.G., Drasdo, D. In vitro to in vivo acetaminophen hepatotoxicity extrapolation using classical schemes, pharmacodynamic models and a multiscale spatial-temporal liver twin. Front. Bioeng. Biotechnol. 11: 1049564 (2023).
Duffield, J.S., Forbes, S.J., Constandinou, C.M., Clay, S., Partolina, M., Vuthoori, S., Wu, S., lang, R., Iredale, J.P. Selective depletion of macrophages reveals distinct, opposing roles during liver injury and repair. J. Clin. Invest. 115(1): 56--65 (2005).
Dutta-Moscato, J., Solovyev, A., Mi, Q., Nishikawa, T., Soto-Gutierrez, A., Fox, I.J., Vodovotz, Y. A multiscale agent-based in silico model of liver fibrosis progression. Frontiers in Bioengineering and Biotechnology 2: 18 (2014).
Ferruzzi, J., Sun, M., Gkousioudi, A., Pillar, A., Roblyer, D., Zhang, Y., Zaman, M.H. Compressive remodeling alters fluid transport properties of collagen networks - implications for tumor growth. Scientific Reports 9: 17151 (2019).
Filliol, A., Saito, Y., Nair, A., Dapito, D.H., Yu, L., Ravichandra, A., Bhattacharjee, S., Affo, S., Fujiwara, N., Su, H., Sun, Q., Savage, T.M., Wilson-Kanamori, J.R., Caviglia, J.M., Chin, L., Chen, D., Wang, X., Caruso, S., Kang, J.K., Amin, A.D., Wallace, S., Dobie, R., Yin, D., Rodriguez-Fiallos, O.M., Yin, C., Mehal, A., Izar, B., Friedman, R.A., Wells, R.G., Pajvani, U.B., Hoshida, Y., Remotti, H.E., Arpaia, N., Zucman-Rossi, J., Karin, M., Henderson, N.C., Tabas, I., Schwabe, R.F. Opposing roles of hepatic stellate cell subpopulations in hepatocarcinogenesis. Nature 610(7931): 356--365 (2022).
Friedman, A., Hao, W. Mathematical model of liver fibrosis. Mathematical Biosciences & Engineering 14(1): 143--164 (2017).
Ghafoory, S., Breitkopf-Heinlein, K., Li, Q., Scholl, C., Dooley, S., Woelfl, S. Zonation of nitrogen and glucose metabolism gene expression upon acute liver damage in mouse. PLoS One 8(10): e78262 (2013).
Ghallab, A., Myllys, M., Holland, C.H., Zaza, A., Murad, W., Hassan, R., Ahmed, Y.A., Abbas, T., Abdelrahim, E.A., Schneider, K.M., Matz-Soja, M., Reinders, J., Gebhardt, R., Berres, M., Hatting, M., Drasdo, D., Saez-Rodriguez, J., Trautwein, C., Hengstler, J.G. Influence of liver fibrosis on lobular zonation. Cells 8(12): 1556 (2019).
Ghosh, S., Kaplan, K.J., Schrum, L.W., Bonkovsky, H.L. Chapter Five – cytoskeletal proteins: shaping progression of Hepatitis C virus-induced liver disease. International Review of Cell and Molecular Biology 302: 279—319 (2013).
Grabher, C., Cliffe, A., Miura, K., Hayflick, J., Pepperkik, R., Rørth, P., Wittbrodt, J. Birth and life of tissue macrophages and their migration in embryogenesis and inflammation in medaka. Journal of Leukocyte Biology 81(1): 263—271 (2007).
Haecker, H., Fuermann, C., Wagner, H., Haecker, G. Caspase-9/-3 activation and apoptosis are induced in mouse macrophages upon ingestion and digestion of Escherichia coli bacteria. J. Immunol. 169: 3172--3179 (2002).
Hammad, S., Hoehme, S., Friebel, A., Von Recklinghausen, I., Othman, A., Begher-Tibbe, B., Reif, R., Godoy, P., Johann, T., Vartak, A., Golka, K., Bucur, O.P., Vibert, E., Marchan, R., Christ, B., Dooley, S., Meyer, C., Ilkavets, I., Dahmen, U., Dirsch, O., Bottger, J., Gebhardt, R., Drasdo, D., Hengstler, J.G. Protocols for staining of bile canalicular and sinusoidal networks of human, mouse and pig livers, three-dimensional reconstruction and quantification of tissue microarchitecture by image processing and analysis. Archives of Toxicology 88: 1161--1183 (2014).
Hammad, S., Braeuning, A., Meyer, C., Mohamed, F., Hengstler, J.G., Dooley, S. A frequent misinterpretation in current research on liver fibrosis: the vessel in the center of CCl_4-induced pseudolobules is a portal vein. Arch. Toxicol. 91(11):3689-3692 (2017).
Hernandez-Gea, V., Friedman, S.L. Pathogenesis of liver fibrosis. Annu. Rev. Pathol. 6: 425--456 (2011).
Higashi, T., Friedman, S.L., Hoshida, Y. Hepatic stellate cells as key target in liver fibrosis. Adv Drug Deliv. Rev. 121:27--42 (2017).
Hoehme, S., Brulport, M., Bauer, A., Bedawy, E., Schormann, W., Hermes, M., Puppe, V., Gebhardt, R., Zellmer, S., Schwarz, M., Bockamp, E., Timmel, T., Hengstler, J.G., Drasdo, D. Prediction and validation of cell alignment along microvessels as order principle to restore tissue architecture in liver regeneration. Proc. Natl Acad Sci USA 107(23): 10371--10376 (2010).
Hoehme, S., Hammad, S., Boettger, J., Begher-Tibbe B., Bucur, P., Vibert, E., Gebhardt, R., Hengstler, J.G., Drasdo, D. Digital twin demonstrates significance of biomechanical growth control in liver regeneration after partial hepatectomy. iScience 26(1): 105714 (2023).

Huang, H., Chang, M., Chen, Y., Hsu, H., Chiang, C., Cheng, T., Wu, Y., Wu, M.Z., Hsu, Y., Shen, C., Lee, C., Chuang, Y., Hong, C., Jeng, Y., Chen, P., Chen, H., Lee, M. Persistent elevation of hepatocyte growth factor activator inhibitors in cholangiopathies affects liver fibrosis and differentiation. Hepatology 55(1): 161--172 (2012).
Iredale, J.P., Benyon, R.C., Pickering, J., McCullen, M., Northrop, M, Pawley, S., Hovell, C., Arthur, M.J. Mechanisms of spontaneous resolution of rat liver fibrosis. Hepatic stellate cell apoptosis and reduced hepatic expression of metalloproteinase inhibitors. The Journal of Clinical Investigation 102(3): 538--549 (1998).
Itoh, M., Suganami, T., Kato, H., Kanai, S., Shirakawa, I., Sakai, T., Goto, T., Asakawa, M., Hidaka, I., Sakugawa, H., Ohnishi, K., Komohara, Y., Asano, K., Sakaida, I., Tanaka, M., Ogawa, Y. CD11c+ resident macrophages drive hepatocyte death-triggered liver fibrosis in a murine model of nonalcoholic steatohepatitis. JCI Insight 2(22): e92902 (2017).
Karabassi, E., Papaioannou, G., Theoharis, T., Boehm, A. Intersection test for collision detection in particle systems. Journal of Graphics Tools 4(1): 25—37 (1999).
Kim, M., Siberberg, Y.R., Abeyaratne, R., Asada, H.H. Computational modeling of three-dimensional ECM-rigidity sensing to guide directed cell migration. Proc. Natl Acad Sci USA 115(3): E390--E399 (2018).
Kisseleva, T., Cong, M., Paik, Y., Scholten, D., Jiang, C., Benner, C., Iwaisako, K., Moore-Morris, T., Scott, B., Tsukamoto, H., Evans, S.M., Dillmann, W., Glass, C.K., Brenner, D.A. Myofibroblasts revert to an inactive phenotype during regression of liver fibrosis. Proc. Natl Acad Sci USA 109(24): 9448--53 (2012).
Kisseleva, T., Brenner, D. Molecular and cellular mechanisms of liver fibrosis and its regression.
Nat. Rev. Gastroenterol. Hepatol. 18(3):151-166 (2021).
Krenkel, O., Tacke, F. Liver macrophages in tissue homeostasis and disease. Nature Rev. Immunol. 17: 306--321 (2017).
Krenkel, O., Hundertmark, J., Ritz, T.P., Weiskirchen, R., Tacke, F. Single cell RNA sequencing identifies subsets of hepatic stellate cells and myofibroblasts in liver fibrosis. Cells 8(5): 503 (2019).
Lara, J., Lopez-Labrador, F.X., Gonzalez-Candelas, F., Berenguer, M., Khudyakov, Y.E. Computational models of liver fibrosis progression for hepatitis C virus chronic infection. BMC Bioinformatics 15(8):S5 (2014).
Levick, J.R. Flow through interstitium and other fibrous matrices. Quarterly Journal of Experimental Physiology 72(4): 409--437 (1987).
Lopez-De Leon, A., Rojkind, M. A simple micromethod for collagen and total protein determination in formalin-fixed paraffin-embedded sections. J. Histochem Cytochem 33(8): 737–743 (1985).
Madsen, D.H., Leonard, D., Masedunskas, A., Moyer, A., Jürgensen, H.J., Peters, D.E., Amornphimoltham, P., Selvaraj, A., Yamada, S.S., Brenner, D.A., Burgdorf, S., Engelholm, L.H., Behrendt, N., Holmbeck, K., Weigert, R., Bugge, T.H. M2-like macrophages are responsible for collagen degradation through a mannose receptor-mediated pathway. Journal of Cell Biology 202(6): 951—966 (2013).
Manssor, N.A.S., Radzi, Z., Yahya, N.A., Yusof, L.M., Hariri, F., Khairuddin, N.H., Kasim, N.H.A., Czernuszka, J.T. Characteristics and Young's modulus of collagen fibrils from expanded skin using anisotropic controlled rate self-inflating tissue expander. Skin Pharmacology and Physiology 29(2): 55--62 (2016).
Martin-Murphy, B.V., Holt, M.P., Ju, C. The role of damage associated molecular pattern molecules in acetaminophen-induced liver injury in mice. Toxicology Letters 192: 387--394 (2010).
Moon, H., Cho, K., Shin, S., Kim, D.Y., Han, K., Ro, S.W. High risk of hepatocellular carcinoma development in fibrotic liver: role of the Hippo-YAP/TAZ signaling pathway. International Journal of Molecular Sciences 20: 581 (2019).
Odenthal, T., Smeets, B., Van Liedekerke, P., Tijskens, E., Van Oosterwyck, H., Ramon, H. Analysis of initial cell spreading using mechanistic contact formulations for a deformable cell model. PLoS Computational Biology 9(10): e1003267 (2013).
Papachristoforou, E., Ramachandran, P. Macrophages as key regulators of liver health and disease. Int. Rev. Cell Mol. Biol. 368: 143--212 (2022).
Parola, M., Pinzani, M. Liver fibrosis: pathophysiology, pathogenetic targets and clinical issues. Molecular Aspects of Medicine 65: 37--55 (2019).
Pinzani, M., Rombouts, K. Liver fibrosis: from the bench to clinical targets. Dig. Liver Dis. 36(4): 231--242 (2004).
Pinzani, M., Luong, T.V. Pathogenesis of biliary fibrosis. Biochimica et Biophysica Acta - Molecular Basis of Disease 1864 (4): 1279--1283 (2018).

Popov, V.L. Contact mechanics and friction. Springer (2010).
Pradere, J., Kluwe, J., De Minicis, S., J, J.J., Gwak, G.Y., Dapito, D.H., Jang, M.K., Guenther, N.D., Mederacke, I., Friedman, R., Dragomir, A., Alomen, C., Schwabe, R.F. Hepatic macrophages but not dendritic cells contribute to liver fibrosis by promoting the survival of activated hepatic stellate cells in mice. Hepatology 58(4): 1461--1473 (2013).
Ramachandran, P., Pellicoro, A., Vernon, M.A., Boulter, L., Aucott, R.L., Ali, A., Hartland, S.N., Snowdon, V.K., Cappon, A., Gordon-Walker, T.T., Williams, M.J., Dunbar, D.R., Manning, J.R., Van Rooijen, N., Fallowfield, J.A., Forbes, S.J., Iredale, J.P. Differential Ly-6C expression identifies the recruited macrophage phenotype, which orchestrates the regression of murine liver fibrosis. Proc Natl Acad Sci USA. 109(46): E3186-95 (2012).
Ribeiro, F.O., Gomez-Benito, M.J., Folgado, J., Fernandes, P.R., Garcia-Aznar, J.M. Computational model of mesenchymal migration in 3D under chemotaxis. Computer Methods in Biomech. Biomed. Eng. 20(1): 59--74 (2016).
Rocha, A.S., Vidal, V., Mertz, M., Kendall, T.J., Charlet, A., Okamoto, H., Schedl, A. The angiocrine factor Rspondin3 is a key determinant of liver zonation. Cell Reports 13(9): P1757--1764 (2015).
Ronceray, P., Broedersz, C.P., Lenz, M. Fiber networks amplify active stress. Proc. Natl Acad Sci USA 113(11): 2827--2832 (2016).
Roohani, S., Tacke, F. Liver injury and the macrophage issue: molecular and mechanistic facts and their clinical relevance. Int. J. Mol. Sci. 22(14): 7249 (2021).
Seki, E., Brenner, D.A. Recent advancement of molecular mechanisms of liver fibrosis. J. Hepatobiliary Pancreat Sci. 22(7): 512--518 (2015).
Seki, E., Schwabe, R.F. hepatic inflammation and fibrosis: functional links and key pathways. Hepatology 61(3): 1066--1079 (2015).
Sekine, S., Lan, B.Y., Bedolli, M., Feng, S., Hebrok, M. Liver-specific loss of -catenin blocks glutamine synthesis pathway activity and cytochrome p450 expression in mice. Hepatology 43(4): 817--825 (2006).
Seo, Y.S., Kwon, J.H., Yaqoob, U., Yang, L., De Assuncao, T.M., Simonetto, D.A., Verma, V.K., Shah, V.H. HMGB1 recruits hepatic stellate cells and liver endothelial cells to sites of ethanol-induced parenchymal cell injury. Am. J. Physiol. Gastrointest. Liver Physiol. 305: G838--G848 (2013).
Shi, C., Jia, T., Mendez-Ferrer, S., Hohl, T.M., Serbina, N.V., Lipuma, L., Leiner, I., Li, M.O., Frenette, P.S., Pamer, E.G. Bone marrow mesenchymal stem and progenitor cells induce monocyte emigration in response to circulating Toll-like receptor ligands. Immunity 34(4): 590—601 (2011).
Soille, P. Morphological image analysis: principles and applications (Vol. 2, No. 3). Berlin: Springer (1999).
Stein, A.M., Vader, D.A., Jawerth, L.M., Weitz, D.A., Sander, L.M. An algorithm for extracting the network geometry of three-dimensional collagen gels. Journal of Microscopy 232: 463--475 (2008).
Sternberg, S.R. Grayscale morphology. Computer vision, graphics, and image processing, 35(3): 333-355 (1986).
Tangkijvanich, P., Tam, S.P., Yee, J.F. Wound-induced migration of rat hepatic stellate cells is modulated by endothelin-1 through Rho-kinase-mediated alterations in the acto-myosin cytoskeleton. Hepatology 3(1): 74—80 (2001).
Teutsch, H.F. The modular microarchitecture of human liver. Hepatology 42(2): 317--325 (2005).
Török, N., Fan, W., Adebowale, K., Li, Y., Rabbi, M.F., Vancza, L., Chen, D., Kunimoto, K., Mozes, G., Li, Y., Tao, J., Monga, S., Charville, G., Wells, R., Dhanasekaran, R., Kim, T., Chaudhuri, O. Extracellular matrix viscoelasticity drives liver cancer progression in pre-cirrhotic NASH. preprint (2022).
Wake, K. Hepatic stellate cells: Three-dimensional structure, localization, heterogeneity and development. Proceedings of the Japan Academy, Series B 82(4): 155—164 (2006).
Wang, Y., Jiang, J. A two-dimensional (2D) systems biology-based discrete liver tissue model: A simulation study with implications for ultrasound elastography of liver fibrosis. Computers in Biology and Medicine 104: 227--234 (2019).
Yang, L., Fitie, C.F.C., Van der Werf, K.O., Bennink, M.L., Dijkstra, P.J., Feijen, J. Mechanical properties of single electrospun collagen type I fibres. Biomaterials 29: 955--962 (2008).
Yang, Y., Liao, J., Lin, C., Chang, C., Wang, S., Ju, M. Characterization of cholesterol-depleted or -restored cell membranes by depth-sensing nano-indentation. Soft Matter 8(3): 682--687 (2012).
Yang, K., Lu, C., Zhao, X., Kawamura, R. From bead to rod: Comparison of theories by measuring translational drag coefficients of micron-sized magnetic bead-chains in Stokes flow. PLoS ONE 12(11): e0188015 (2017).
Van Liedekerke, P., Palm, M.M., Jagiella, N., Drasdo, D. Simulating tissue mechanics with agent-based models: concepts,

perspectives and some novel results. Computational Particle Mechanics 2: 401--444 (2015).
Van Liedekerke, P., Neitsch, J., Johann, T., Alessandri, K., Nassoy, P., Drasdo, D. Quantitative cell-based model predicts mechanical stress response of growing tumor spheroids over various growth conditions and cell lines. PLoS Computational Biology 15(3): e1006273 (2019).
Van Liedekerke, P., Neitsch, J., Johann, T., Warmt, E., Gonzalez-Valverde, I., Hoehme, S., Grosser, S., Kaes, J., Drasdo, D. A quantitative high-resolution computational mechanics cell model for growing and regenerating tissues. Biomechanics and Modeling in Mechanobiology 19: 189--220 (2020).
Wells, R.G. How collagen becomes 'stiff'. Elife 11: e77041 (2022).
Wen, Y. The role of immune cells in liver regeneration. Livers 3(3): 383--396 (2023).
Wenger, M.P., Bozec, L., Horton, M.A., Mesquida, P. Mechanical properties of collagen fibrils. Biophysical journal 93(4): 1255--1263 (2007).
Winkler, B., Aranson, I.S., Ziebert, F. Confinement and substrate topography control cell migration in a 3D computational model. Communications Physics 2: 82 (2019).
Winkler, M., Staniczek, T., Kuerschner, S.W., Schmid, C.D., Schoenhaber, H., Cordero, J., Kessler, L., Mathes, A., Sticht, C., Nessling, M., Uvarovskii, A., Anders, A., Zhang, X., Figura, G., Hartmann, D., Mogler, C., Dobreva, F., Schledzweski, K., Geraud, C., Koch, P., Goerdt, S. Endothelial GATA4 controls liver fibrosis and regeneration by preventing a pathogenic switch in angiocrine signaling. Journal of Hepaotycte 74: 380--393 (2021).
Wong, F.W., Chan, W.Y., Lee, S.S. Resistance to carbon tetrachloride-induced hepatotoxicity in mice which lack CYP2E1 expression. Toxicol. Appl. Pharmacol. 153(1): 109--118 (1998).
Wu, L., Zhang, Q., Mo, W., Feng, J., Li, S., Li, J., Liu, T., Xu, S., Wang, W., Lu, X., Yu, Q., Chen, K., Xia, Y., Lu, J., Xu, L., Zhou, Y., Fan, X., Guo, C. Quercetin prevents hepatic fibrosis by inhibiting hepatic stellate cell activation and reducing autophagy via the TGF-β1/Smads and PI3K/Akt pathways. Sci. Rep. 7(1): 9289 (2017).
Zaher, H., Buters, J.T., Ward, J.M., Bruno, M.K., Lucas, A.M., Stern, S.T., Cohen, S.D., Gonzalez, F.J. Protection against acetaminophen toxicity in CYP1A2 and CYP2E1 double-null mice. Toxicol. Appl. Pharmacol. 152(1): 193--199 (1998).
Zandarashvili, L., Sahu, D., Lee, K., Lee, Y.S., Singh, P., Rajarathnam, K., Iwahara, J. Real-time kinetics of high-mobility group box 1 (HMGB1) oxidation in extracellular fluids studied by in Situ protein NMR spectroscopy. Journal of Biological Chemistry 288(17): 11621—11627 (2013).
Zellmer, S., Schmidt-Heck, W., Godoy, P., Weng, H., Meyer, C., Lehmann, T., Sparna, T., Schormann, W., Hammad, S., Kreutz, C., Timer, J., Weizsacker, F., Thurmann, P.A., Merfort, I., Guthke, R., Dooley, S., Hengstler, J.G., Gebhardt, R. Transcription factors ETF, E2F, and SP-1 are involved in cytokine-independent proliferation of murine hepatocytes. Hepatology 52(6): 2127--2136 (2010).
Zhao, J., Ghallab, A., Hassan, R., Dooley, S., Hengstler, J.G., Drasdo, D. A digital twin of liver predicts regeneration after drug-induced damage at the level of cell type orchestration. Submitted (2023).

Acknowledgements

The authors acknowledge the support of the Core Facility for Imaging, Medical Faculty Mannheim, Heidelberg University, and the data storage service SDS@hd supported by the Ministry of Science, Research and the Arts Baden-Württemberg and the German Research Foundation.

Funding

This study was supported by the BMBF (German Federal Ministry of Education and Research) Project LiSyM (Grant PTJ-FKZ: 031L0043 and 031L0045), LiSyM Cancer (Grant PTJ-FKZ: 031L0257A and 031L0257D), ANR iLite, ANR-16-RHUS-0005, DFG grant INST 35/1503-1 FUGG, DFG project number: 259332240 - RTG/GRK 2099, 394,046,768 - CRC/SFB 1366; 314,905,040 - CRC/SFB-TR 209; 413,262,200 - ICON/EB 187/8-1.

Competing interests

The authors declare no competing interests.

Author contributions

SH conceived animal studies, blood analysis, and RNA isolation. PE, SH and YL performed RT-PCR, and IHC staining, as well as manual image analysis. MW, SWK, PSK performed animal experiments in GATA4$^{LSEC\text{-}KO}$ mice. MDL and NG performed an automated image analysis. JZ and DD designed and developed the DT model. JZ implemented the code and performed simulations and visualized the results. PVL and AB provided the original code of DCM and collagen model. SH and JZ wrote the manuscript. MPE, JGH, SD, and DD performed critical revision of the manuscript. SD, SH and DD acquired funding for this study. All authors read the final version of the manuscript.